12-2013

# Investigation of Composite Patch Performance Under Low-Velocity Impact Loading

Geoffrey Roy Goodmiller
*University of Tennessee - Knoxville*, ggoodmil@utk.edu

To the Graduate Council:

I am submitting herewith a thesis written by Geoffrey Roy Goodmiller entitled "Investigation of Composite Patch Performance Under Low-Velocity Impact Loading." I have examined the final electronic copy of this thesis for form and content and recommend that it be accepted in partial fulfillment of the requirements for the degree of Master of Science, with a major in Civil Engineering.

Stephanie C. TerMaath, Major Professor

We have read this thesis and recommend its acceptance:

Edwin G. Burdette, Richard M. Bennett

Accepted for the Council:
Carolyn R. Hodges

Vice Provost and Dean of the Graduate School

(Original signatures are on file with official student records.)

# Investigation of Composite Patch Performance

# Under Low-Velocity Impact Loading

A Thesis Presented for the
Master of Science
Degree
The University of Tennessee, Knoxville

Geoffrey Roy Goodmiller
December 2013

# ACKNOWLEDGEMENTS

First and foremost, I would like to thank Dr. Stephanie TerMaath for her support, guidance, patience, and encouragement throughout this last year without which this research would have been impossible. I am especially grateful that she offered me the opportunity and support to conduct this research. Through her assistance, I have been able develop my skills at finite element analysis, visit with industry professionals, and tour manufacturing sites. I am so glad to have had this experience.

I also want to thank Dr. Bennett and Dr. Burdette for being on my thesis committee. I want to give special thanks to Dr. Burdette for talking me into continuing my education in graduate school and to Dr. Bennett, Prof. White, and Prof. Schleter for supporting me for my first year of graduate school. Additionally, I want to thank Melanie Smith for her assistance in digitizing experimental data and Jonathan Weigand for his assistance in determining lamina properties from fiber and matrix material properties.

Finally, I want to thank Cristina Ruffner for her patience, love, devotion, and grammar assistance during this last year and a half. I would not have made it through graduate school without her.

# ABSTRACT

Bonded fiber composite repair on damaged metal structures can be an effective method to restore load carrying capacity or increase damage resistance. Low velocity impacts can cause barely visible damage to the interior structure of laminated composites. Delamination between plies is of particular concern in these composites. Impacts may also create disbonds between the patch and metal substrate. A building-block approach was suggested to model impact damage to composite patches. Composite, adhesive, and metal substrate damage models were separately validated and then combined. Cohesive Zone theory modeled interlaminar composite damage and adhesive damage. Hashin failure criteria with energy dissipation based damage evolution modeled intralaminar damage to the composite. The Johnson-Cook plasticity model captured the metal substrate's behavior. A full model of a hybrid composite-metal system was then assembled and validated. Finally, a sensitivity study was performed that found that increasing ply thickness and fiber content improved composite patch impact damage resistance.

# TABLE OF CONTENTS

# LIST OF TABLES

# LIST OF FIGURES

# CHAPTER I

# INTRODUCTION

## 1.1 Composite Patch Repair

Fiber reinforced polymer (FRP) composite patches are adhesively bonded to a metallic structure as a repair method to either restore the load carrying capacity of a damaged structure or to increase damage tolerance in an undamaged structure as reinforcement. This patch forms a hybrid structure consisting of the metal surface, the composite patch, and an adhesive which bonds the two together (Figure 1). The composite may be optimized to carry load in one direction with only 0° plies, or it may provide reinforcement in multiple directions by including plies of other orientation, typically 45°, 90°, or interwoven. The adhesive transfers loads between metal and composite and provides a stiff connection due to its large area for load transfer, despite its own relatively low stiffness [1].

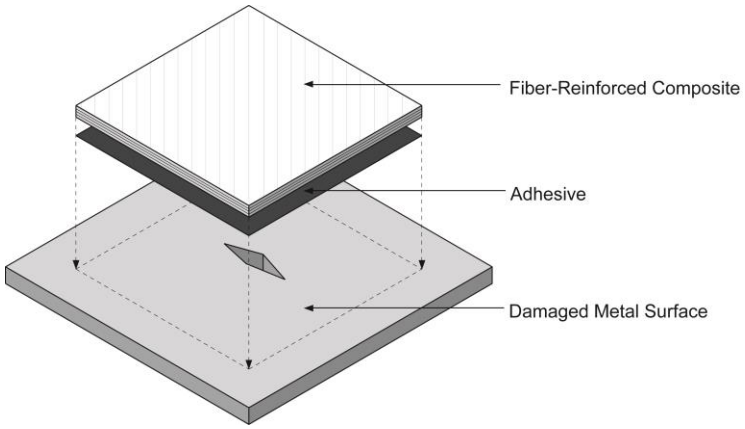


**Figure 1. Anatomy of a composite patch**

FRP composite patch repairs have several potential advantages over the more traditional methods of bolting or welding of metal plates onto metallic structures:

- Fibers within the composite may be arranged in a position, density, and orientation within the matrix to optimize material properties in the directions corresponding to loading conditions;
- Per unit volume, composite materials weigh much less than metal (but may require larger volumes), generally making transport and handling easier;
- FRP composites have high failure strain and durability;
- Composite patches are more easily formed to unusual surfaces than steel plates;
- Composites have high corrosion resistance;
- Adhesive bonding prevents stress concentrations at bolt holes.

However, composite patches also have some associated disadvantages when compared to traditional bolted or welded repairs:

- Composites have a 4-20 times higher unit volume cost than steel;
- The customizability and complexity of the material makes design more difficult;
- Performance is very dependent on the skill of the installer;
- Performance is also dependent on bonding surface. Uneven surfaces may lead to peeling, and chemical treatment may be necessary to produce a clean, chemically active surface for the adhesive;
- Composites have brittle failure modes;
- The adhesive can suffer environmental degradation, including the effects of water intrusion;
- Matrix hardening can cause cracking at sub-zero temperatures;

- Thermal coefficients in the metal and composite material are often mismatched, leading to stresses and separation;
- Impacts may cause barely visible or unseen damage to the composite.

Despite these disadvantages, bonded composite repairs to metallic structures are being applied in an increasingly broad spectrum of disciplines, including aerospace, naval, and civil engineering [2, 3].

An area of particular concern in the continued strength and performance of a composite bonded repair is the effect of impact damage on a hybrid structure. A low-velocity impact, such as a tool drop, can cause visually undetectable damage to a composite's interior structure that can initiate failure. Low-velocity impact damage may take the form of matrix cracking, fiber breakage, or delamination between plies. Delamination in particular can drastically reduce the composite's load-carrying capacity, especially in compression, as susceptibility to buckling is increased with the separation of the plies [4]. This strength reduction from damage also hampers the patch's effectiveness in transferring and carrying loads from the damaged metal underneath. Similarly, an impact may create a disbond between the composite and steel layers by damaging the adhesive layer.

## 1.2 Research Objectives

Little research into the combined low-velocity impact damage resistance of the composite-metal patch is available in published literature. However, the deleterious effects of low-velocity impact damage on the mechanical performance of a composite plate are well-known. The potential for a visually undetectable combination of this composite damage with probable adhesive damage suggests that low-velocity impact

damage in composite to metal bonded repair should be researched and considered during design. Performing physical experiments to quantify impact damage on composite patches is expensive and difficult considering the number of different parameters to be considered and the internal nature of the damage. Finite element analysis (FEA) provides a more cost effective way to predict and assess damage in composite patches, as well as providing an avenue to explore many material combinations and configurations. FEA can then illuminate the areas where limited experimental testing may be necessary for validation and clarification of damage behavior.

Many input parameters are important to the impact performance of the hybrid structure: patch shape; constitutive properties of all three materials; number, orientation, and thickness of plies in the composite; thickness and initial damage condition of the metallic structure; quality of the bond surface; differing coefficients of thermal expansion of composite and metal; and damage tolerance properties of the three materials. Damage mechanics of the patch are also critical to understanding patch performance; these mechanics include amount and type of degradation in the composite structure (matrix cracking, matrix crushing, fiber breakage, delamination, etc.), disbonds between metal and composite, load redistributions between parts, and stresses induced at the edge of composite patch. To ensure reliable and optimized patch design, understanding the effects of multiple input uncertainties, damage mechanics, and their interactions is imperative.

The goal of this research was to conduct a FEA which captured the damage mechanisms pertinent to the performance of a composite patch on an undamaged metal surface under low-velocity impact loading. The data gathered from this simulation was

compared to available experimental data in quantitative terms of absorbed energy, contact force, and maximum deflection, and qualitative measures such as delamination shape and size, and composite damage location and type. The research used Abaqus 6.12, which provided built-in models for composite damage, metal plastic behavior, and cohesive zone theory.

Due to the limited availability of experimental data on composite patch performance and the sometimes obscure material properties needed for damage models, several assumptions were made to create the validation hybrid model. These include assumptions of material strengths, ply thicknesses, and steel properties. Once experimental data validated the hybrid model, a parameter study was performed to identify the sensitivity of the model to several of these uncertain input factors.

In addition to validating assumptions made during modeling, studying these parameters is important to arriving at an optimum composite patch configuration and material selection for impact damage resistance. Other potentially sensitive factors such as fiber/matrix material, ply orientation, number of plies, patch size, patch shape, metal thickness, metal damage, adhesive type, and thermal expansion mismatch were not examined in this study, but should be investigated in future work.

## 1.3 Overview of Technical Approach

While no published numerical analyses were identified through a literature review on impact damage to composite bonded repair of metal structures, FEA techniques are commonly used with good results to model impact on composites and metals, as well as to model adhesive disbonds and composite delamination. Consequently, the model for this research was developed using a building-block approach, separately simulating and

validating impact damage in models of the composite and metal layers and disbonding in the adhesive layer. These separate, validated models were then assembled as a hybrid plate, which was validated against experimental results. Once validated, parameters within the finite element model were changed to perform a sensitivity analysis.

### *Composite Approach*

Impact damage to the composite portion of the hybrid can be characterized as intralaminar (matrix or fiber tension or compression damage within each ply) or interlaminar (delamination occurring between plies). To facilitate both damage regions, each composite ply was modeled separately with a single element through thickness. Intralaminar damage was simulated based on a continuum damage mechanics (CDM) approach, which was implemented through the Hashin failure criteria and damage evolution model provided by Abaqus and described in Lapczyk & Hurtado [5]. This model describes a constitutive model for unidirectional fiber-reinforced composites with fiber and matrix failure criteria based on Hashin's failure criteria [6] and damage evolution based on the model suggested by Camanho et al. [7]. This model provides output detailing matrix tension, matrix compression, fiber tension, and fiber compression damage within each ply, which each reduce the stiffness of damaged components.

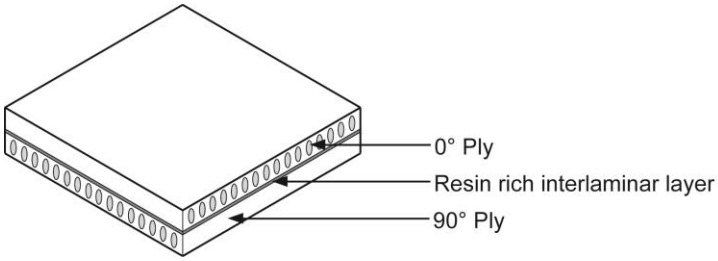


**Figure 2. Diagram of resin-rich layer between plies**

The resin-rich area between plies where delamination occurs, depicted in Figure 2, was modeled using thin layers of cohesive elements between each ply. Cohesive Zone Theory governs the behavior of these elements, using traction-separation laws for elastic behavior and the Benzeggah-Kenane (BK) mixed-mode law [8] for damage and failure behavior. These cohesive element layers were tied to the ply layers above and below them; as the cohesive elements failed and were deleted, the plies became unbound, representing a delamination.

Turon's method [9] for reducing the required mesh size in cohesive zones was employed. Due to the uncertain nature of the material properties and inherent mesh size dependence in the application of cohesive zone theory, a series of finite element simulations of double-cantilever beam (DCB) tests, benchmarking Mode I fracture behavior, and mixed-mode bending (MMB) tests, benchmarking combined Mode I and II fracture, were performed to study and validate mesh size, penalty stiffness, and interface strength.

Upon validating the material property inputs for the cohesive elements, the composite model was assembled and subjected to a low-velocity impact. The energy absorption, maximum deflection, and damage patterns were compared to experimental values for validation of the above methods.

### *Adhesive Approach*

The adhesive layer was also modeled with cohesive elements. However, the thickness of the adhesive layer was not negligible as it had been in the interlaminar damage model. Additionally, the high Mode II ductility of the adhesive required an investigation of the shape of the governing traction-separation curve. A comparison of

DCB tests and end-notched flexure (ENF) FEA results to experimental data validated the adhesive properties.

### *Metal Approach*

The Johnson-Cook plasticity and damage models available in Abaqus 6.12 captured the behavior of metal under a low-velocity impact [10]. This damage model accounts for strain-rate effects, temperature, plastic behavior and fracture damage within a metal. Results from a low-velocity impact on a thin metal plate were compared to experimental values for validation.

### *Hybrid Model Approach*

After each individual component was validated, a hybrid model was created by assembling the three materials. The adhesive layer was tied to the composite above and the metal surface below. The patch was assumed to cover the entire metal surface. Upon validation, a series of tests varying the patch thickness and fiber orientation were performed. The sensitivity of the model to these parameters was quantified by comparing the results in deflection, energy absorption, and contact force in the validation and altered models. This thesis provides the results and details of this hybrid model.

# CHAPTER II

# LITERATURE REVIEW

## 2.1 Hybrid/Repair Patch Applications

The practice of repairing a damaged metal structural member with a fiber-reinforced composite patch is becoming more widespread among multiple engineering disciplines. Patches are currently being used or investigated for use in applications that range from aircraft and naval vessels to bridges and structures.

### *Aerospace Industry Applications*

The aerospace industry pioneered the use of bonded composite patches for repair of metallic structures. Military aircraft have been successfully repaired with composite patches for years, and the commercial aircraft industry is beginning to incorporate the technology as well [11]. Cracks in aircraft structure typically occur due to repeated fatigue loading at areas of stress concentration, such as bolt holes, areas of stress-corrosion, and material defects. The growth of these cracks can have severe repercussions on the lifespan of an aircraft. Composite patches have been used to repair secondary and tertiary structures, and, more recently, primary structures. Residual stresses, caused by the mismatch between thermal expansion coefficients are a major consideration in aerospace composite patch design [1].

A few of the many examples of composite patch repair in the aerospace industry are described as follows. Callinan and Galea investigated the acoustic failure of a composite bonded repair to the F/A-18, and their research suggested that adding damping materials such as Soundcoat Dyad 606 would drastically reduce crack growth

vs. undamped or unpatched panels [12]. Chester described the reinforcement of the Royal Australian Air Force F-111 wing pivot fitting with a boron/epoxy composite, reducing strain in that part by 30% [13]. Bartholomeusz et al. developed a rapid repair technique with carbon/vinyl ester patches on aircraft battle damage, in order to quickly restore damaged planes to airworthiness in times of conflict. Experimental work indicated that the bonded composite battle damage repair performed better than traditional fastened repairs under both static and fatigue loading [14].

### *Civil Engineering Applications*

Civil engineers are beginning to examine the use of composite repair patches for rehabilitating failing structures. Hollaway and Cadei [3] noted that a major area of interest is in bridge repair; bridge structures are deteriorating due to corrosion from increasing use of de-icing salt and fatigue from modern traffic exceeding the design load capacities of older bridges. For failing structures such as these, rehabilitation is usually a more attractive option than demolition. Hollaway and Cadei [3] also provided an overview of all relevant properties and considerations of composite patch repair of bridges, and they described several examples of work that has already been completed, such as the I-704 Bridge, in Newark, Delaware and the Bow Road Bridge in East London.

Metallic structures pose several unique problems for composite patches. Lateral buckling necessitates composite steel structures where the compression flange is constantly supported by reinforced concrete. Steel's higher modulus of elasticity than CFRP implies that for a given strain, the CFRP is working at lower stress. Finally, the adhesive bond, often the weakest link in the hybrid system, introduces the possibility of brittle failure modes [3].

Many other researchers have conducted studies into the reinforcement of steel structures with composite patches. Colombi et al. [15] studied the use of pre-stressed composite patches to repair cracked steel sections and prevent fatigue damage. Leveraging this research as validation for the repair of riveted steel bridges, Colombi et al. strongly recommended pretension for future composite bridge repairs. Schnerch et al. [16] proposed a set of design guidelines for the strengthening of steel bridge girders with composite patches based on best practices described in the literature and in the field. Shaat et al. [17] addressed the repair of corroded or notched steel girders and the strengthening of undamaged beams with composite patches. Also addressed in Shaat's research were the durability, fatigue behavior, bond force and transfer mechanism, and galvanic corrosion of hybrid composite structures. Zhao et al. [18] studied the bond between FRP and steel, strengthening hollow steel sections, and fatigue-crack propagation. Bocciarelli et al. and Colombi et al. both studied fatigue performance of unconditioned, double-sided reinforcement under tension, focusing on stiffness degradation due to adhesive disbonding [19, 20]. Teng et al. reviewed and interpreted the current literature on strengthening steel structures with FRP composites [21].

### *Naval Applications*

Composite patches are also used in naval and marine applications. Grabovac and Whittaker [22] described the carbon fiber patches installed on a Royal Australian Navy frigate to inhibit fatigue cracking on the superstructure 15 years before the study. These patches were found to be effective in restoring the strength of the damaged structure; repairs were cost effective and non-disruptive to ship activities. The patches also proved to be durable, lasting all 15 years on a weather-deck, and were repairable, easily inspected, and easily removed.

Turton et al. [23] described patch repairs to Type 21 frigates, Type 42 destroyers, offshore drilling platforms, and other marine structures. For example, composite patches were used to arrest and repair fatigue cracks in aluminum superstructures of the Type 21 frigates, especially on the weather-decks, in 1982. After success on one ship, the superstructures on all seven Type 21 frigates were patched whether they were cracked or not. No further cracking was subsequently found under these patches, and the ships were still in service as of 2005.

Composite patches were also used to repair leaking oil tanks on an offshore oil platform in Norway. A welded repair would have required a complete emptying of all tanks within two bulkheads of the leaking tank as a result of the volatility of the contents. Due to the low curing temperature of the composite patch, only the offending tank had to be emptied to accommodate composite patch repair, saving time and money [23].

Shamsuddoha et al. [24] conducted a review of research into composite repair of underwater steel pipes. Their investigation found that repairs of corroded or gouged pipes were promising but required more research before wide-scale implementation.

## 2.2 Impact Damage in Composites

Predicting the impact damage behavior of composites is complicated by the propensity of the material to fail in multiple modes simultaneously. The failure modes that must be captured by any successful damage model include matrix cracking, fiber-matrix disbond, fiber fracture, and delamination of ply layers [25, 26]. Properties of the composite that may affect impact behavior include material properties of the fiber and matrix, fiber orientation within the plies, number of plies, thickness of plies, manufacturing defects, whether the plies are unidirectional or woven, and the presence

of stitching or z-pinning. Malik et al. [27] performed a sensitivity study on unstitched, unidirectional composites which showed that thickness and ply orientation had the largest effect on damage resistance to low-velocity impact and that the longitudinal tensile strength of the fiber was most important among material properties. Damage is also affected by the size, shape, mass, velocity and material properties of the impactor [28].

Many experimental tests have been performed to characterize the damage progression of composites under low-velocity impact loading. Belingardi et al. [29] noted three general outcomes for low velocity impacts, which were characterized by the final behavior of the impactor: rebound, partial penetration, or complete perforation. Lopes et al. [30] described the general dynamics of the impact event. As the impactor strikes, its kinetic energy is initially transferred to the composite plate as elastic strain energy. When an ultimate material strength is reached somewhere within the composite, elastic strain energy begins to dissipate through permanent damage. As the impactor's velocity reaches zero, all its kinetic energy has either been transformed to elastic strain energy or dissipated through damage. If elastic strain energy remains, the impactor and plate deformations reverse and accelerate in the opposite direction, transforming this strain energy back into kinetic energy and causing the impactor to rebound. The plate then continues to vibrate, dissipating more energy. If elastic strain energy has been entirely dissipated through damage and vibration, the impactor has penetrated the composite and will either remain in place or perforate the plate if sufficient kinetic energy remains [30].

Evci and Gulgec [31] described in detail the qualitative damage progression of several types and configurations of E-glass/epoxy composites under each of these

impact outcomes. In each case, two distinct points on the load-time curve can be identified and tied to specific forms of damage. Impact damage typically begins with the first sudden drop in the load on the load-time curve, known as Hertzian failure, which occurs due to the first onset of delamination. After the Hertzian failure, the stiffness of the composite is noticeably reduced. Shyr and Pan [26] noted that the magnitude of the force at the Hertzian failure point is primarily a function of laminate thickness. The second key point on the load-time curve is the maximum force, which corresponds to the first intra-lamina failure. Upon reaching this point, the force oscillates until the maximum impact energy is reached and the impact force begins to decrease [31].

For low impact energies, the energy dissipated by the impact is less than the initial kinetic energy of the impactor, which leads to a rebound. Minor cracks develop in the matrix due to compression in the top surface, while fiber straining is evident at the bottom due to bending stresses. A delamination of increasing size appears on the bottom face. Interior delaminations also develop in the interfaces between plies of different orientations, increasing in size from the top layer to the bottom [31]. Large delaminations are most likely between plies with the greatest difference in fiber angles, as these interfaces develop the highest interlaminar shear stresses [30]. The direction and shape of each delamination is dependent upon the ply fiber orientation. Delamination is the primary failure mode for low impact energies leading to rebound [26].

With higher initial impact energies, the impactor will partially penetrate the composite. In the event of penetration, damage on the top surface is limited to the punching damage in an area roughly the size of the diameter of the impactor. Matrix crushing and fiber crushing and breakage occur in this area directly under the impactor due to high stresses [31]. A permanent indention may be created by matrix cracking and

fiber breakage; a 1 mm indention is considered the threshold for the damage to be considered “Barely Visible” [30]. Matrix cracks spread from the top downward, inclined at about 45°, and interconnect with interlaminar delamination, which leaves an undamaged cone-shaped area directly under the impactor. Matrix cracking and fiber breakage develop under the undamaged cone on the bottom face due to bending stresses [26]. The growth of delamination in penetration cases is more limited when compared to the rebound cases, as damage primarily takes the form of fiber breakage [31].

During an impact leading to perforation, the combination of total possible energy dissipation and elastic strain energy is less than the initial impact energy. As the impactor passes through the composite plate, it dissipates some energy through material fragmentation and Coulomb friction while maintaining some kinetic energy [29]. Damage behavior in this case is primarily dominated by fiber breakage; delamination sizes are smaller than in rebound or partial penetration cases [31]. Perforation marks the upper bound of what is considered a low-velocity impact, and it falls outside the scope of this research.

## 2.3 Impact Modeling of Composites

The low-velocity impact behavior of composite structures has been extensively researched and modeled. Most recent FEA approaches for modeling low-velocity impact damage on a composite plate use a ply-by-ply method in which each ply is modeled separately with an interface layer inserted between plies to capture delamination. These methods generally rely on CDM to represent intralaminar damage. CDM, pioneered by Kachnakov [32], represents cracks and other micro-scale damage

as smeared damage which degrades the material stiffness of an element [33] . The particular CDM model employed varies from study to study, though it is often at least partially based on the Hashin 1980 failure criteria [6]. Delamination between these plies is modeled using variations of fracture mechanics, occasionally with the virtual crack closure technique (VCCT) or, more often, with cohesive zone modeling (CZM) [34]. While this approach generally produces accurate results, the computational power and time required are frequently a hindrance.

Malik et al. [27] performed a sensitivity analysis on various design parameters. In this study, low-velocity impact performance depended most on plate thickness and stacking sequence, while the elastic moduli of the fibers and matrix had less effect than the strength of the fiber and matrix materials. This study used Hashin damage criteria for intralaminar damage; it did not separately model delamination.

Kim et al. [35] developed a damage progression law using a Weibull distribution to compute composite strength and modified Hashin failure criteria. Shear failure criteria were replaced with strain energy criteria for simulating nonlinear shear behavior. Shear damage was considered separately by maximum strain criteria. Cohesive elements with BK mixed-mode damage evolution modeled delamination.

In order to reduce computation time, Guiamatsia et al. [36] used enriched finite elements to increase mesh size while maintaining proper damage behavior. Laminate damage was captured by the two-dimensional orthotropic damage model of Iannucci and Ankerson. Results were accurate, but no savings in computational time were reported.

Shi et al. [37] employed the Hashin failure criteria for fiber and tensile damage, the Puck model [38] for matrix compressive damage, cohesive elements with BK criteria

for delamination, and the semi-empirical model in Berbinau et al. [39] for nonlinear shear. Results showed good agreement between the size, shape, and location of damage.

Raimondo et al. [40] modeled delamination without cohesive elements by using fracture based 3-D damage criteria to predict the 3-D orientation of cracks. These criteria allowed ply elements to also simulate delamination as a particular orientation of a matrix crack. This method allowed for multiple cracks per element, but it required a crack density parameter. The sizes, but not shapes, of delaminations were captured.

Gonzalez et al. [41] studied the effects of ply clustering in low-velocity impacts. Their research found that clustering plies of the same orientation together did not significantly affect the strength of the material in compression after impact testing. Ply clustering did lead to longer impact times and larger delaminations between plies of different orientations.

## 2.4 Disbonds between Composite and Metal

The effect of low-velocity impacts on the adhesive between the composite patch and metal has not been widely published, though several papers have mentioned impact as a possible initiator of disbond [42]. As delaminations in composites tend to occur between plies of differing orientations due to interlaminar shear stresses, so might disbonds be expected to occur in a brittle adhesive between the composite and metal substrate due to their differing impact behaviors. Soutis et al. [43] found these interlaminar shear stresses to be a concern for patch disbonding in damaged composites repaired with composite patches. However, Baker [44] notes that the structural adhesives typically used in aircraft repair have significantly higher toughness

than most composites; fatigue failure often begins near the surface of the composite rather than within the adhesive layer.

Research has been conducted exploring other factors affecting disbonds in patches. Denney and Mall [45] studied disbonds in repaired cracked aluminum panels caused by air pockets. They found the location of the disbond to be important in determining its effect on patch performance; disbonds occurring over cracks resulted in greater crack growth and fatigue damage than disbonds occurring a distance away from cracks. Al-Zubaidy et al. [46] conducted experiments on the bond strength between CFRPs and steel with epoxy adhesive under impact tensile loading; their research indicates that bond strength increases with increasing loading rates until offset by the onset of delamination within the CFRP. Fatigue loading is another common source of disbond propagation in adhesively bonded joints [47].

## 2.5 Impact on Hybrid Structures

Few studies have been published to date on the effect of a low-velocity impact on a composite patch on a metal substrate. The research that has been done focuses on experimental results and has been performed primarily on unidirectional CFRP and GFRP composites.

Charpy V-notch tests were performed on edge notched steel plates repaired on each side by Kevlar/epoxy or glass/epoxy; Glass/epoxy patches failed by fiber pull-out, while Kevlar/epoxy patches failed by adhesion failure and slippage. The Kevlar/epoxy patches absorbed more energy [48]. Charpy tests were also performed on one-sided repairs of edge notched aluminum plates; carbon patches were found to be more

effective than glass. Increasing the number of layers slightly increased energy absorption [49].

Williams et al. [50] performed low-velocity impact tests on carbon/epoxy composite bonded to undamaged, plasma treated 18 gage (1.2 mm) steel plates and on steel plates alone. Results indicated considerable reduction in impact depth, from 7 mm to 4 mm at 78.9 J and from 1 mm to 0.1 mm at 2.7 J, as well as damage area, from 19.6 mm to 0.8 mm at 78.9 J and from 1.1 mm to 0.1 mm at 2.7 J. Composite configurations were not provided.

Helms et al. [51] tested 34 unidirectional and cross-ply laminates bonded to steel plates with epoxy cement at six different impact energies. The addition of the composite improved the stiffness and impact resistance of the metal substrate. Plate configurations were not provided.

Akimoto et al. [52] studied low-velocity impacts on steel clad with chopped strand mat, bi-axial unidirectional glass-fiber reinforced plastic (GFRP), and quasi-axial unidirectional GFRP. The GFRP was tested without steel backing, rested on steel backing, and adhered to steel backing at 4, 8, and 12 J impact energies. The addition of steel was found to increase the maximum force and absorbed energy, even more when epoxy adherent was added.

Akimoto et al. [53] further studied impact on carbon-fiber reinforced plastic (CFRP) and GFRP adhered with either an epoxy or an ionomer to stainless steel plates. Impacts were conducted at 10 J and 120 J with two different sizes of hemispherical strikers on bi-axial and quasi-axial samples. They found that maximum load increased in the GFRP samples with increased striker size and decreased in the CFRP samples.

Delaminations and surface fiber breakages were more pronounced on bi-axial samples. Ionomer, a soft adhesive, resisted disbond better than the brittle epoxy adhesive.

## 2.6 Impact on Fiber-Metal Laminates

Fiber-Metal laminates (FML), created through the layering of fiber composites with thin metal sheets, compose a related class of hybrid structure. Sometimes FMLs are composed of metal sheets as the exterior layers with composites within; often the FML has interior metal layers as well. In some respects, a composite patch on a thin metal structure could be considered mechanically similar to a FML. The key differences separating composite patches and FMLs are as follows: (a) the patch and metal are not a single product manufactured under tightly controlled processes, and they are thus more likely to have imperfect bonding; (b) the thicker bond between the metal and the composite in a patch cannot be neglected when considering performance; (c) the metal sheets of an FML are often much thinner than the metal substrate under a patch; (d) the outermost layer of an FML is not usually a composite; (e) various considerations such as patch size, shape, and edge conditions have no meaning for a FML. A benefit of the FML is that impact damage is very visible due to deformations in the metal surface [54]. Despite these differences, many of the behaviors and models governing impact damage to an FML are the same as for a composite patch.

Fan et al. [55] used the Hashin damage criteria to study perforation in a woven fiber laminate section and rate-dependent stress strain curves to model aluminum for impact on a FML composed of alternating layers of woven GFRP and aluminum. Delamination between composite plies, adhesion, and separation of composite and metal were not modeled. Their model successfully predicted perforation energy.

Lapczyk et al. [5] developed a model for predicting FML failure using CDM. Hashin criteria were employed as failure criteria, with damage evolution based on critical fracture energies for the four Hashin damage modes proposed by Maimi et al. [56]. Metal damage was represented by isotropic strain hardening curves, while the adhesive was modeled using a triangular traction separation law. This research defined the progressive failure model for fiber composites implemented in Abaqus.

Nakatani et al. [57] studied low-velocity impact on titanium/GFRP hybrid laminate experimentally and numerically. Large disbonds and separations between metal and composite were noted. The researchers observed that the titanium layers seemed to prevent damage to the GFRP core. FEA included damage evolution based on the Hashin criteria for composites, the Johnson-Cook plasticity model for titanium, and cohesive elements with traction/separation laws for the adhesives.

Reyes and Cantwell [58] conducted experiments on aluminum/glass-fiber reinforced polypropylene. Their research indicated that combining the plastic deformation of the aluminum with cracking in the composite allowed significant increases in energy absorption over traditional composites in low-velocity impacts. Tensile tests on 4/3 lamina specimens damaged in 20 J impacts showed only a 15% reduction in strength.

Zhu and Chai [54] conducted numerical and experimental tests on low-velocity impacts on FML panels consisting of GFRP sandwiched between layers of aluminum. They tested both unidirectional and woven laminas. Zhu's FEA consisted of Johnson-Cook plasticity and damage models for metal and Hashin criteria for both woven and unidirectional lamina. Nodes of the GFRP and aluminum were tied together; disbonding was not considered. They found that when an FML reached its load limit, the metal layer

would yield; this yielding was marked by large plastic deformations, which then caused excessive strain and failure in GFRP layers. The FML totally failed when the metal layer reached its fail strain.

This thesis leveraged this research by adopting an approach to composite modeling similar to that found in much of the current research. Plies were modeled individually with a CDM approach to damage, while delamination was modeled with cohesive elements. Adhesive and metal damage were handled with approaches similar to those described for FMLs. Johnson-Cook plasticity laws were used for the metal, and cohesive elements with traction-separation behavior were used for the adhesive. These approaches were applied to the particular problem of a composite bonded patch for which no FEA examples were discovered during the literature review.

# CHAPTER III

# DAMAGE MODEL VALIDATIONS

## 3.1 Introduction

In order to construct the hybrid composite model, damage models for the unidirectional composite, metal, and adhesive layers were selected and validated independently. In the case of the composite and metal, different materials than those needed for the final hybrid validation were used to validate the individual damage models due to the availability of experimental data. The adhesive validated in this chapter was the same adhesive used in the hybrid model validation.

The composite was constructed using two distinct damage models. One model captured ply damage, while the other model captured delamination between plies. CZM simulated delamination; this damage model was independently validated due to the uncertain nature of the material properties used therein. Cohesive layer validation, which consisted of comparing DCB and MMB load-deflection curves to theoretical solutions, was performed for both carbon/epoxy and E-glass/epoxy composites. The intralaminar damage was modeled using the Hashin failure criteria; it was not validated independent of the impact. These two models were then combined into a full laminate model of a unidirectional E-glass/epoxy composite subjected to a low-velocity impact. Experimental data validated this combination in terms of absorbed energy, contact force, and damage patterns.

The metal damage model, a strain rate dependent Johnson-Cook plasticity model, was validated under a low-velocity impact in terms of maximum deflection and

deflection shape. Aluminum was tested due to the ready availability of low-velocity impact data for thin aluminum plates.

The adhesive was also modeled using CZM, similar to delamination within the composite. Araldite 2015, a ductile epoxy adhesive, was validated for Mode I and Mode II fracture behavior by comparing load deflections curves of DCB and ENF specimens against experimental data in order to arrive at appropriate damage models for the cohesive elements.

## 3.2 Intralaminar Damage Model

***Selection of Damage Model***

A CDM approach in which cracks are represented as smeared damage which degrades the stiffness of an element modeled damage within composite plies. The advantage of a CDM approach over a micromechanical approach (trying to predict and represent individual cracks in the material) is a reduction in complexity and computational intensity. Most CDM approaches for composite materials consist of two critical components: failure criteria that determine the conditions under which damage initiates and a damage evolution model that controls the degradation of element stiffness and ultimately element deletion. The failure criteria can be stress or strain based, while damage evolution is usually computed as a function of either fracture energy release or ultimate strain.

Hashin [6] suggested stress-based failure criteria that separately account for failure in fiber tension, fiber compression, matrix tension, and matrix compression in order to represent the different material behavior for failure modes such as fiber rupture, fiber buckling, matrix cracking, and matrix crushing. These individual criteria are based

on a combination of theory and experimental curve-fitting. The damage modes are dependent on local material orientations. Fiber tension and compression correspond to material properties in the longitudinal direction, conventionally noted as direction 1. Matrix tension and compression are the primary damage modes in the transverse direction (denoted as 2). No damage modes for the out-of-plane direction (3) are postulated. Refer to Figure 3 for a graphic representation of these conventions.

The resulting Hashin failure criteria are widely used in industry and research [6]. However, several studies have demonstrated that these criteria do not always fit experimental data, especially for matrix and fiber compression. For example, experimental data shows that transverse compression increases the apparent shear strength of a ply. This effect is not captured by Hashin's criteria. Neither does Hashin's fiber compression criteria account for strength reduction due to the effects of in-plane shear [59]. Despite these flaws, the Hashin criteria are still often applied to composite modeling due to their ease of usage and general accuracy. For these reasons and their implementation as the progressive damage model for fiber composites in Abaqus, this study used the Hashin 1980 failure criteria.

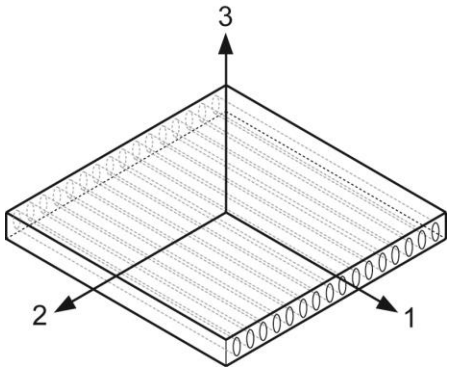


**Figure 3. Local lamina element orientation convention**

The application and evolution of progressive damage in Abaqus is specifically based on the model proposed by Lapczyk & Hurtado [5] which combines Hashin failure criteria with Bažant and Oh's crack band theory [60], Camanho and Davila's damage evolution [34], and Matzenmiller's model for computing the degradation of the stiffness matrix [61]. This damage model is valid for plane stress elements, such as continuum shells.

***Failure Criteria***

The Hashin plane stress failure criteria in this research are as follows [6]:

Tensile fiber mode ($\hat{\sigma}_{11} \geq 0$):

$$\left(\frac{\hat{\sigma}_{11}}{X_t}\right)^2 + \left(\frac{\hat{\sigma}_{12}}{S_L}\right)^2 = 1 \tag{1}$$

Compressive fiber mode ($\hat{\sigma}_{11} \leq 0$):

$$\left(\frac{\hat{\sigma}_{11}}{X_c}\right)^2 = 1 \tag{2}$$

Tensile matrix mode ($\hat{\sigma}_{22} \geq 0$):

$$\left(\frac{\hat{\sigma}_{22}}{Y_t}\right)^2 + \left(\frac{\hat{\sigma}_{12}}{S_L}\right)^2 = 1 \tag{3}$$

Compressive matrix mode ($\hat{\sigma}_{22} \leq 0$):

$$\left(\frac{\hat{\sigma}_{22}}{2S_T}\right)^2 + \left[\left(\frac{Y_c}{2S_T}\right)^2 - 1\right]\frac{\hat{\sigma}_{22}}{Y_c} + \left(\frac{\hat{\sigma}_{12}}{S_L}\right)^2 = 1 \tag{4}$$

In these equations, $X_t$ and $X_c$ represent the longitudinal tensile and compressive strength, $Y_t$ and $Y_c$ represent the transverse tensile and compressive strengths, and $S_L$ and $S_T$ represent the longitudinal and transverse shear strengths. $\hat{\sigma}_{ij}$ represents the effective stress in the corresponding direction.

Lapczyk introduced damage variables, $d_f^t$, $d_f^c$, $d_m^t$, and $d_m^c$, whose values range from 0 at or before damage initiation in a given mode to 1 at complete failure in that mode. These values are combined to determine damage variables for matrix, fiber, and shear ($d_m$, $d_f$, and $d_s$):

$$d_m = \begin{cases} d_m^t & \text{if } \hat{\sigma}_{22} \geq 0 \\ d_m^c & \text{if } \hat{\sigma}_{22} < 0 \end{cases} \tag{5}$$

$$d_f = \begin{cases} d_f^t & \text{if } \hat{\sigma}_{11} \geq 0 \\ d_f^c & \text{if } \hat{\sigma}_{11} < 0 \end{cases} \tag{6}$$

$$d_s = 1 - \left(1 - d_f^t\right)\left(1 - d_f^c\right)(1 - d_m^t)(1 - d_m^c) \tag{7}$$

These damage variables are then used in damage operator, **M:**

$$\mathbf{M} = \begin{bmatrix} \frac{1}{(1-d_f)} & 0 & 0 \\ 0 & \frac{1}{(1-d_m)} & 0 \\ 0 & 0 & \frac{1}{(1-d_s)} \end{bmatrix} \tag{8}$$

This matrix is applied to the true stress tensor, $\boldsymbol{\sigma}$, to determine the effective stress tensor, $\hat{\boldsymbol{\sigma}}$:

$$\hat{\boldsymbol{\sigma}} = \mathbf{M}\boldsymbol{\sigma} \tag{9}$$

If the material is completely undamaged, **M** is equal to the identity matrix. The effective stress tensor is used by Abaqus in calculating the Hashin damage initiation criteria, as denoted in Equations 1 to 4.

### *Damage Evolution*

Lapczyk based damage evolution on a generalization of the cohesive damage evolution model proposed by Camanho and Davila [34]. The Hashin failure criteria control the initiation of damage within an element.

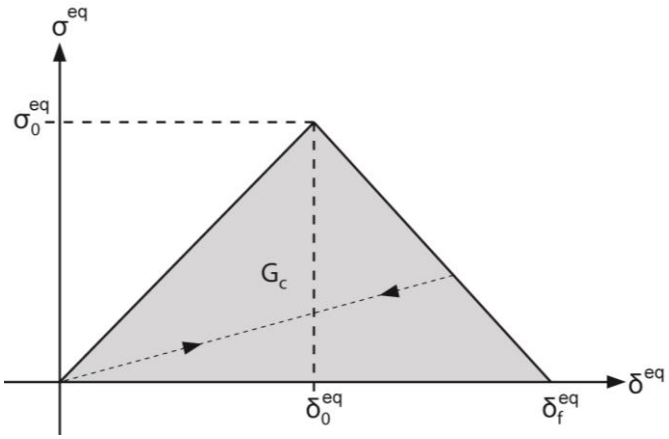


**Figure 4. General stress-displacement curve for lamina damage**

The damage variables previously described are computed from equivalent stresses and displacements. The equivalent stress and displacement behavior for each of the four modes of failure is based on the bi-linear curve shown in Figure 4. The material behavior is linear elastic for the first section of the curve, until the equivalent stress is such that the failure criterion (Eqs. 1 to 4) reaches 1. At this point, $\delta_0^{eq}$ denotes equivalent displacement, and $\sigma_0^{eq}$ denotes equivalent stress. The equivalent failure displacement, $\delta_f^{eq}$, is calculated from the area of the triangle, $G_c$, a material parameter that represents the energy dissipated by failure for a given mode. The section of the curve from $\delta_0^{eq}$ to $\delta_f^{eq}$ represents softening behavior as the material undergoes damage. Unloading at any point along the portion of the curve corresponding to damage follows a straight path back to the origin.

The introduction of a characteristic length ($L_c$) allows a definition of damage evolution through displacement rather than strain. Based on Bažant and Oh's crack band theory, this adjustment alleviates the problem of mesh dependency [60]. Without this adjustment, energy dissipation is proportional to the volume of the element; as the

mesh is refined, the energy dissipated approaches zero. However, introducing a characteristic length allows the fail strain to vary in order to keep $G_c$ constant by the relationship [5]:

$$\varepsilon^f = \frac{2G_c}{\sigma_c L_c} \tag{10}$$

For a shell element, $L_c$ is computed as the square root of the area of the reference surface. As noted, this method reduces mesh dependency, though a maximum mesh size was suggested by Maimi et al. [56]. Similarly using crack band theory, Maimi suggested $L_c$ be limited by the following relationship:

$$L_c \leq \frac{2E_M G_M}{X_M^2} \tag{11}$$

In this equation $E_M$, $G_M$, and $X_M$ are the Young's modulus, critical fracture energy, and strength of the composite respectively, for a given damage mode.

A different energy dissipation rate exists for each of the four damage modes. Maimi et al. [56] provided a description of experimental and theoretical formulations for these energy dissipation parameters. However, results from the tests described are neither easily available in the literature, nor are they results of common experimentation. Thus, assumptions must often be made for these values, as in Lapczyk & Hurtado.

The equivalent stress-displacement relationship is governed by the following equations, in which $\varepsilon_{ij}$ represents the strain in the *ij* direction [5]:

Fiber tension:

$$\delta_{ft}^{eq} = L^c \sqrt{\langle \varepsilon_{11} \rangle^2 + \varepsilon_{12}^2} \tag{12}$$

$$\sigma_{ft}^{eq} = \frac{\langle \sigma_{11} \rangle \langle \varepsilon_{11} \rangle + \sigma_{12}\varepsilon_{12}}{\delta_{ft}^{eq}/L^c} \tag{13}$$

Fiber compression:

$$\delta_{fc}^{eq} = L^c\langle -\varepsilon_{11}\rangle \tag{14}$$

$$\sigma_{fc}^{eq} = \frac{\langle -\sigma_{11}\rangle\langle -\varepsilon_{11}\rangle}{\delta_{fc}^{eq}/L^c} \tag{15}$$

Matrix tension:

$$\delta_{mt}^{eq} = L^c\sqrt{\langle \varepsilon_{22}\rangle^2 + \varepsilon_{12}^2} \tag{16}$$

$$\sigma_{mt}^{eq} = \frac{\langle \sigma_{22}\rangle\langle \varepsilon_{22}\rangle + \sigma_{12}\varepsilon_{12}}{\delta_{mt}^{eq}/L^c} \tag{17}$$

Matrix compression:

$$\delta_{mc}^{eq} = L^c\sqrt{\langle -\varepsilon_{22}\rangle^2 + \varepsilon_{12}^2} \tag{18}$$

$$\sigma_{mc}^{eq} = \frac{\langle -\sigma_{22}\rangle\langle -\varepsilon_{22}\rangle + \sigma_{12}\varepsilon_{12}}{\delta_{mc}^{eq}/L^c} \tag{19}$$

The Macaulay brackets, $\langle\ \rangle$, are defined such that $\langle x\rangle = (x + |x|)/2$. For any given mode, the corresponding damage variable ($d_f^t$, $d_f^c$, $d_m^t$, and $d_m^c$) is given by:

$$d = \frac{\delta_f^{eq}\left(\delta_{max}^{eq} - \delta_0^{eq}\right)}{\delta_{max}^{eq}\left(\delta_f^{eq} - \delta_0^{eq}\right)} \tag{20}$$

In Equation 20, $\delta_{max}^{eq}$ refers to the maximum displacement reached during loading. As seen in Figure 4, future unloading and reloading behavior is dependent on the maximum displacement reached by the material. The actual material damage response, after damage initiation, is calculated from the strain matrix ( $\boldsymbol{\varepsilon}$) and degraded stiffness matrix ($\mathbf{C_d}$), as proposed by Matzenmiller et al. [61] and incorporated into Lapczyk's model:

$$\boldsymbol{\sigma} = \mathbf{C_d}\boldsymbol{\varepsilon}, \tag{21}$$

where,

$$\mathbf{C_d}=\frac{1}{D}\begin{bmatrix}(1-d_f)E_1 & (1-d_f)(1-d_m)\nu_{21}E_1 & 0\\ (1-d_f)(1-d_m)\nu_{12}E_2 & (1-d_m)E_2 & 0\\ 0 & 0 & (1-d_s)GD\end{bmatrix} \quad (22)$$

$$D = 1-(1-d_f)(1-d_m)\upsilon_{12}\upsilon_{21} \quad (23)$$

The damage variables ($d_m$, $d_f$, and $d_s$) within $\mathbf{C_d}$ are the same as those used in **M** for calculating failure criteria.

***Material Properties***

Typical material properties for the E-glass/epoxy composite lamina used in the following sections are provided in Table 1. These properties were determined experimentally from E-glass/epoxy composites with a fiber volume ratio of 60%. The previously unmentioned variables used in Table 1 are defined as follows: $E_i$, Young's modulus in the *i* direction; $\nu_{ij}$, Poisson's ratio in the *ij* direction; $G_{ij}$, shear modulus in the *ij* direction; and $\varepsilon_{it}$ and $\varepsilon_{it}$ , failure strain in the *i* direction in tension and compression respectively. Transverse shear strength is calculated using Eq. A1 in Appendix A.1. The energy dissipation rates ($G_f^t$, etc.) are estimated by assuming a critical length of 1 and using the appropriate strength and fail strain in Equation 10.

**Table 1. Material properties for E-glass/epoxy lamina ($V_f$ = 0.60)**

| Property | Units | Value | Source |
|---|---|---|---|
| $\rho$ | g/cc | 1.8 | [31] |
| $E_1$ | GPa | 45.6 | [62] |
| $E_2$ | GPa | 16.2 | [62] |
| $E_3$ | GPa | 16.2 | [62] |
| $\nu_{12}$ | - | 0.278 | [62] |
| $\nu_{13}$ | - | 0.278 | [62] |
| $\nu_{23}$ | - | 0.4 | [62] |
| $G_{12}$ | GPa | 5.83 | [62] |
| $G_{13}$ | GPa | 5.83 | [62] |
| $G_{23}$ | GPa | 4.5 | [63] |
| $X_t$ | MPa | 1280 | [62] |
| $X_c$ | MPa | 800 | [62] |
| $Y_t$ | MPa | 40 | [62] |
| $Y_c$ | MPa | 145 | [62] |
| $S_L$ | MPa | 73 | [62] |
| $S_T$ | MPa | 54.8 | [64] |
| $\varepsilon_{1t}$ | % | 2.807 | [62] |
| $\varepsilon_{1c}$ | % | 1.754 | [62] |
| $\varepsilon_{2t}$ | % | 0.246 | [62] |
| $\varepsilon_{2c}$ | % | 1.2 | [62] |
| $G_f{}^t$ | N/mm | 17.965 | [62] |
| $G_f{}^c$ | N/mm | 7.016 | [62] |
| $G_m{}^t$ | N/mm | 0.049 | [62] |
| $G_m{}^c$ | N/mm | 0.870 | [62] |

## 3.3 Interlaminar Damage Model

***Selection of Damage Model***

Cohesive zone theory was selected to simulate delamination between composite plies. This theory applies LEFM to simulate adhesion between two surfaces as cohesive elements with properties independent of the material properties of the adhered surfaces themselves. The properties of the cohesive zone are instead that of the resin-rich area between two unidirectional plies.

Cohesive zone theory has several advantages over other fracture mechanics approaches for the modeling of delamination or adhesion. Cohesive zone theory is more computationally efficient for these applications than stress concentration techniques, since the crack growth is confined to a two dimensional pre-defined cohesive zone. This zone is the only area in which delamination may occur.

Virtual crack closure technique (VCCT), based upon the theory that the energy released by crack propagation equals the work required to return the crack to its original position, has often been employed for delamination studies. In VCCT, nodal forces and displacements are used to compute single mode components of the energy release rate [9]. VCCT assumes that the stress field for an advancing crack is self-similar. VCCT requires very small elements at the crack front demanding either a very fine mesh or adaptive re-meshing techniques throughout the simulation. VCCT also requires an initial flaw be assumed to begin the crack [65].

Cohesive zone modelling (CZM) overcomes the drawbacks of VCCT by placing thin cohesive elements in areas of potential crack growth. These elements are given a material model, which can include both linear elastic and damage softening behavior, based upon traction-separation laws. CZM incorporates fracture mechanics by assuming the area under the softening curve to be equal to the critical fracture energy. Damage initiation is then related to interface strength [65]. In this way, damage leading to delamination can be modeled as smeared damage within the cohesive layer, similar to the intralaminar damage model. This area of material softening, occurring at the crack tip, is known as the cohesive zone [9]. With this technique, CZM reduces the requirement for very small mesh sizes seen in VCCT and does not require an initial flaw, since the crack may begin and spread anywhere within the layer of cohesive elements.

However, using cohesive elements for modeling delamination also has several drawbacks. The most critical drawback is that many cohesive elements must be present across the cohesive zone; at least 3 and up to 10 elements may be required for a good solution. The cohesive zone is often very small (approximately 1 mm for many graphite/epoxy composites), which may lead to extremely fine meshes and significantly increase the required computational time [66]. Another issue is that the inputs for several material properties for cohesive elements are not obvious, especially when defining the stiffness parameter, $K$. Finally, the model may run into convergence problems associated with softening damage models [9].

### *Cohesive Zone Theory*

In this study, cohesive behavior is modeled by traction-separation laws using quadratic stress-based failure criteria and mixed-mode, energy based damage evolution. In a single mode of failure, the traction (*t*) represents the stress in the direction of failure within the cohesive element, while the separation ($\delta$) represents the change in displacement between the top and bottom of the cohesive element. The area under the traction-separation curve represents the critical fracture energy ( $G_c$).

Several constitutive equations exist for predicting the shape of the traction-separation curve, which can range from a trapezoid [67], to polynomial and exponential formulations [9]. However, when only a single failure mode is present during crack growth, the outcome is not sensitive to the shape of the cohesive law. Generally, behavior is sensitive only to the peak stress and area under the curve [67]. For this reason, the bi-linear traction-separation curve (Figure 5) is often used to model single-mode delamination [68].

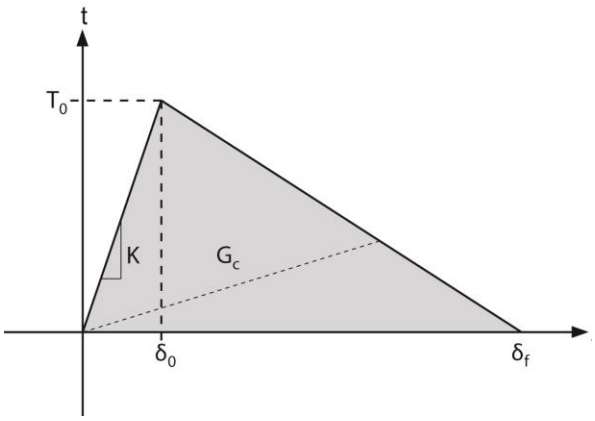


**Figure 5. Bi-linear traction separation law**

In this model a linear elastic range is postulated from 0 to $\delta_0$, which occurs at the maximum traction($T_0$). The slope of this line is defined as the penalty stiffness ($K$). The value of $K$ to be input is neither well supported by theory, nor derived empirically. In general, $K$ must be large enough to provide stiffness to the model, but not so large as to create numerical instabilities in the form of stress oscillations during FEA [9]. Many researchers have postulated formulas for calculating $K$. Turon suggested $K=K_1=K_2=K_3$, where $K$ has the following value:

$$K = \frac{\alpha E_3}{h} \tag{24}$$

In Equation 24, $h$ is the thickness of the adhered plies and $\alpha$ >>1, with a suggested value of 50 [9]. Alternatively, Corigliano suggested:

$$K_1 = \frac{2G_{13}}{e};\ K_2 = \frac{2G_{23}}{e};\ K_3 = \frac{E_3}{e} \tag{25}$$

In Eq. 25, *e* is a fictitious thickness attributed to the interface [69]. Camanho et al. used a penalty stiffness of $K = 10^6$ N/mm$^3$ [7], whereas Harper used $K = 10^5$ N/mm$^3$ [68], both with good results.

Generally, the maximum traction for a given mode is taken as the strength of the adhesive material in that direction. In the case of composite delamination, $T_0 = Y_t$ for Mode I and $S_0 = S_L$ for Mode II as these values correspond roughly to the matrix material strengths in tension and shear. The critical energy release rate, $G_c$, for each mode must be measured experimentally. In a composite, Mode II and Mode III are generally assumed to be identical.

The approximate cohesive length for each mode can be determined from the equations [9, 66]:

$$l_{cz\_I} = ME_2 \frac{G_{Ic}}{T_0^2} \text{ and } l_{cz\_II} = ME_2 \frac{G_{IIc}}{S_0^2} \quad (26, 27)$$

The variable $M$ depends on the cohesive zone theory employed. Possible values for $M$ range from 0.21 [70] to 1.0 [71]. The Hillerborg model, taking $M$ = 1, will be employed in this study as it was in Turon et al. and Song et al. [9, 66]. The cohesive zone length determined from this equation can then be used to size the cohesive zone mesh appropriately. If $N_e$ represents the number of elements in the cohesive zone, and $L_e$ represents the length of each element, then the element length required for Modes I and II must be [66]:

$$l_e \leq \frac{l_{cz_I}}{N_e} \text{ and } l_e \leq \frac{l_{cz_{II}}}{N_e} \quad (28, 29)$$

### *Coarse Mesh Adjustment*

As previously noted, one major drawback in using cohesive elements is that a very fine mesh may be required to provide enough elements within the cohesive zone; this requirement potentially leads to very long run times. To alleviate this problem, Turon et al. [9] proposed an approach for cohesive modeling with a coarse mesh, based on the research of Alfano and Crisfield [72]. Alfano and Crisfield showed that artificially reducing the maximum permitted traction, $T_0$, can reduce the computation burden of cohesive element modeling by allowing for a coarser mesh around the crack tip while maintaining correct material behavior. As long as the crack length is very large compared to the cohesive zone length, LEFM requires that the energy release rate to create a new fracture area must be equal to $G_c$. Thus, if $G_c$ is held constant, the effects of interfacial strengths may be neglected. An expression derived from Equations 26-27 to 28-29 calculates the maximum tractions necessary to accommodate a chosen mesh size and number of elements within the cohesive zone [66]:

$$T^a = \sqrt{\frac{E_2 G_{Ic}}{N_e l_e}} \text{ and } S^a = \sqrt{\frac{E_2 G_{IIc}}{N_e l_e}} \qquad (30, 31)$$

The interface strengths used in FEA should be the minimum of $T^a$ and $Y_t$, and of $S^a$ and $S_L$. Turon noted that when using this coarse mesh adjustment, stress concentrations at the crack tip are generally less accurate [9].

### *Mixed-Mode Damage Model*

When multiple cracking modes are present simultaneously, a mixed mode damage model is necessary to combine their effects (Figure 6). As previously noted, a

common assumption for modeling delamination in composites is that $G_{IIC} = G_{IIIC}$. The BK mixed-mode equation, determined empirically from E-glass/epoxy MMB delamination testing, computes the critical energy($G_C$) based on mixing Mode I and Mode II fracture energies [8]:

$$G_C = G_{IC} + (G_{IIC} - G_{IC})\left(\frac{G_{shear}}{G_T}\right)^{\eta} \tag{32}$$

In this equation, $G_{shear} = G_{II} + G_{III}$, and $G_T = G_I + G_{II} + G_{III}$ [66]. The BK material parameter, $\eta$, is determined by curve fitting experiment data. The critical fracture energy found by the BK equation determines the mixed-mode failure separation, $\delta_f^m$, while the quadratic stress criterion determines the separation at which damage begins, $\delta_0^m$, as seen in Figure 6.

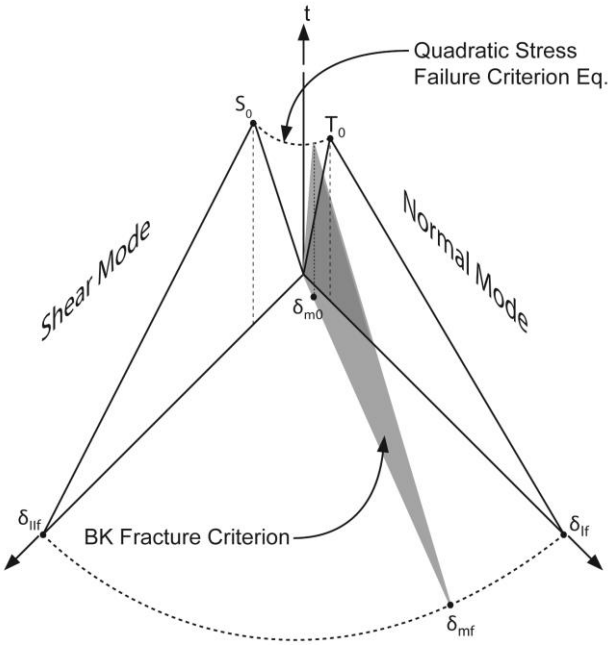


**Figure 6. Diagram of mixed-mode traction-separation model**

***Damage Initiation, Evolution, and Viscosity***

In Abaqus, the values chosen for $K_1$, $K_2$, and $K_3$ govern elastic traction-separation behavior. Damage to a cohesive element is initiated based on failure criteria defined either in terms of stresses or strains; stress criteria were chosen since the values $T_0$ and $S_0$ were easily attainable. The failure criteria may be based on tractions in one fracture mode reaching the interface strength (MAXS) or on a quadratic combination of ratios of tractions to their respective interface strengths (QUADS) [73]. The quadratic traction initiation was selected as it accounts for mode mixing in failure criteria:

$$\left\{\frac{\langle t_n \rangle}{T_0}\right\}^2 + \left\{\frac{t_s}{S_0}\right\}^2 + \left\{\frac{t_t}{S_0}\right\}^2 = 1 \tag{33}$$

The Macaulay brackets indicate that compressive stresses or deformations do not initiate damage. Upon reaching damage initiation, further separation causes irreversible damage. A scalar variable, *D*, represents damage by changing from 0 at damage initiation to 1 at element failure, so that:

$$t_n = (1 - D)\bar{t_n} \tag{34}$$

$$t_s = (1 - D)\bar{t_s} \tag{35}$$

$$t_t = (1 - D)\bar{t_t} \tag{36}$$

In these equations $\bar{t_n}$, $\bar{t_s}$, and $\bar{t_t}$ are stress components predicted by elastic behavior for current strains without damage. An effective mixed-mode displacement is given by [34]:

$$\delta^m = \sqrt{\langle \delta^n \rangle^2 + (\delta^s)^2 + (\delta^t)^2} \tag{37}$$

The damage evolution is then assumed to be linear, such that:

$$D = \frac{\delta_f^m(\delta_{max}^m - \delta_0^m)}{\delta_{max}^m\left(\delta_f^m - \delta_0^m\right)} \tag{38}$$

In Eq. 38 $\delta_f^m$ is the effective displacement at complete failure ($\delta_f^m = 2G_c/T_{eff}^0$ where $T_{eff}^0$ is the effective traction at damage initiation and $G_c$ is from Eq. 32), $\delta_0^m$ is the effective displacement at damage initiation, and $\delta_{max}^m$ refers to the maximum value of effective displacement achieved during load history [34]. Figure 7 graphically represents the definition of the damage variable ($D$), and its application in damage evolution. As in intralaminar damage, unloading follows a linear path back to the origin from the maximum separation reached during loading.

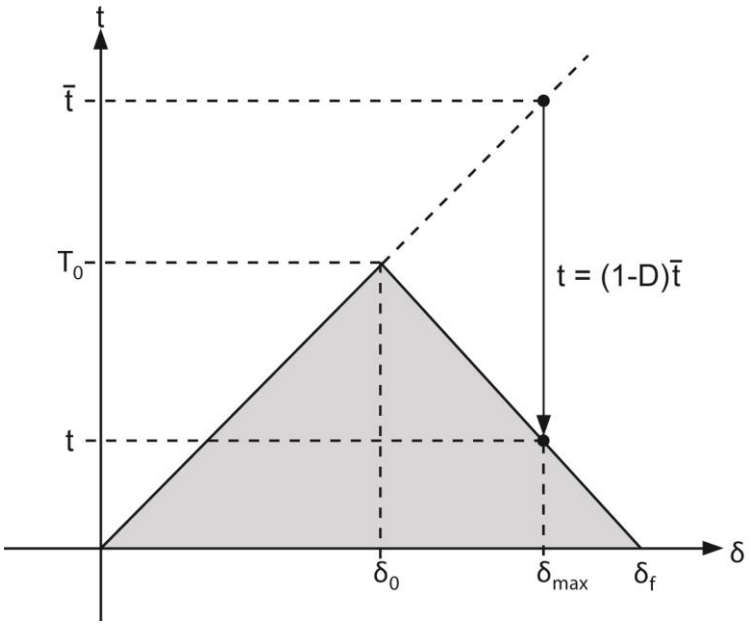


**Figure 7. Calculation and application of damage variable, $D$**

In implicit analyses such as Abaqus/Standard, material softening behavior often leads to convergence problems. Viscous regularization can alleviate these problems. Regularization of traction-separation laws involves the calculation of a viscous stiffness degradation variable, $D_v$ [73].

$$\dot{D_v} = \frac{1}{\mu}(D - D_v) \tag{39}$$

In Eq. 39, $\mu$ represents the relaxation time of the viscous system, and $D$ is the damage variable without considering viscosity. The traction response of the material is given by [73]:

$$\mathrm{t} = (1 - D_v)\bar{t} \tag{40}$$

***Parameter Study & Validation***

Due to the uncertain nature of the inputs for penalty stiffness, interface strength, viscosity in Abaqus/Standard, and mesh size dependence, cohesive element material parameters must be studied and validated before use in a simulation. In this study, the cohesive elements were calibrated by a DCB test that validated pure Mode I behavior and set a general range for the inputs and a MMB test that validated mixed-mode cracking behavior. These validations compared a FEA, based on the analysis by Song et al. [66], against the theoretical solutions for the DCB [65] and MMB [74] provided in Appendix A.2 and A.3 respectively. Upon validating this approach to cohesive elements, material properties were determined and validated for the composite impact model, based on the properties of an E-glass/epoxy composite previously provided in Table 1.

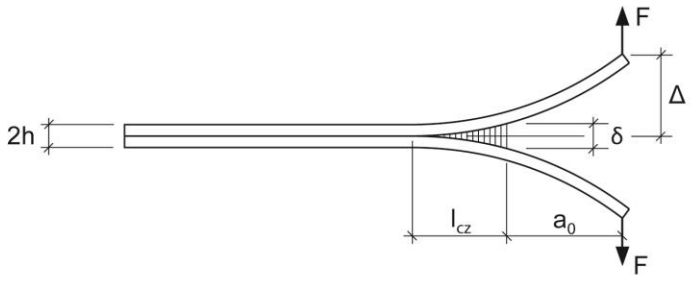


**Figure 8. DCB test setup**

***Double Cantilever Beam Test***

The general configuration of the DCB test is shown in Figure 8. The specimen modeled was 101.6 mm long, 7.62 mm wide, and composed of two 1.524 mm thick laminates with an initial crack length of 29.21 mm [66]. Table 2 provides the material properties used by Song et al. Mesh size, interface strength, penalty stiffness, and element viscosity were varied to determine the most accurate and efficient cohesive element properties. The finite element model consisted of lamina (C3D8R, 8 node, continuum solid, reduced integration elements) joined together by a 0.01 mm thick layer of COH3D8 cohesive elements.

Figure 9 shows the effect of changing the number of elements within the cohesive zone length by lowering the interface strength on the load-deflection curve of the DCB. From these and other tests, the dependence of the interface strength on the penalty stiffness became clear. A number of different combinations of strength and stiffness yielded acceptable results. For example, using a 0.5 mm mesh, $N_e$ = 10, $K$ = 100000, and $\mu$ = 1x10$^{-5}$ yield a solution comparable to the $N_e$ = 3 case depicted in Figure 9.

**Table 2. Material properties for AS4/3501-6**

| Property | Units | Value | Source |
|---|---|---|---|
| $E_1$ | GPa | 148 | [66] |
| $E_2$ | GPa | 10.5 | [66] |
| $E_3$ | GPa | 10.5 | [66] |
| $v_{12}$ | - | 0.27 | [66] |
| $v_{13}$ | - | 0.27 | [66] |
| $G_{12}$ | GPa | 5.61 | [66] |
| $G_{13}$ | GPa | 5.61 | [66] |
| $G_{23}$ | GPa | 3.17 | [66] |
| $Y_t$ | MPa | 53.78 | [66] |
| $S_L$ | MPa | 86.88 | [66] |
| $G_{Ic}$ | kJ/m$^2$ | 0.08 | [66] |
| $G_{IIc}$ | kJ/m$^2$ | 0.55 | [66] |
| $\eta$ | - | 1.8 | [66] |

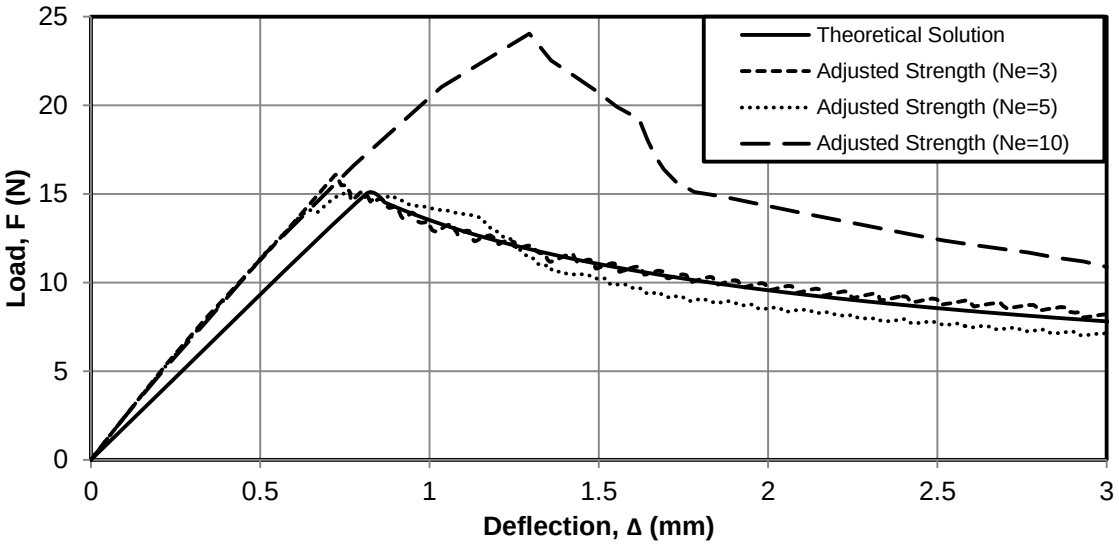


**Figure 9. Effect of interfacial strength on the load-deflection curve for DCB (0.5 mm mesh, $K$ = 100,000; $\mu$ = 0.0001)**

Figure 10 shows the effect of varying $K$ while holding interface strength, mesh size, and viscosity constant, while Figure 11 shows the results of varying only the viscosity variable, $\mu$. Without including the viscosity constant, the FEA quickly diverges and fails. However, too large a viscosity coefficient results in an over-prediction of load carrying capacity, as seen in Figure 11 when $\mu$ = 0.001 or 0.01. Likewise, as the value of $K$ increased, the amount of viscosity needed to stabilize the model decreased; this fact led to the divergent solutions seen for the higher values of $K$ in Figure 10.

Many combinations of these inputs gave converged, accurate results for Mode I fracture. For a given mesh size and interface strength, several combinations of $K$ and $\mu$ worked. Thus, those solutions that performed fastest and worked for mixed-mode bending were preferred.

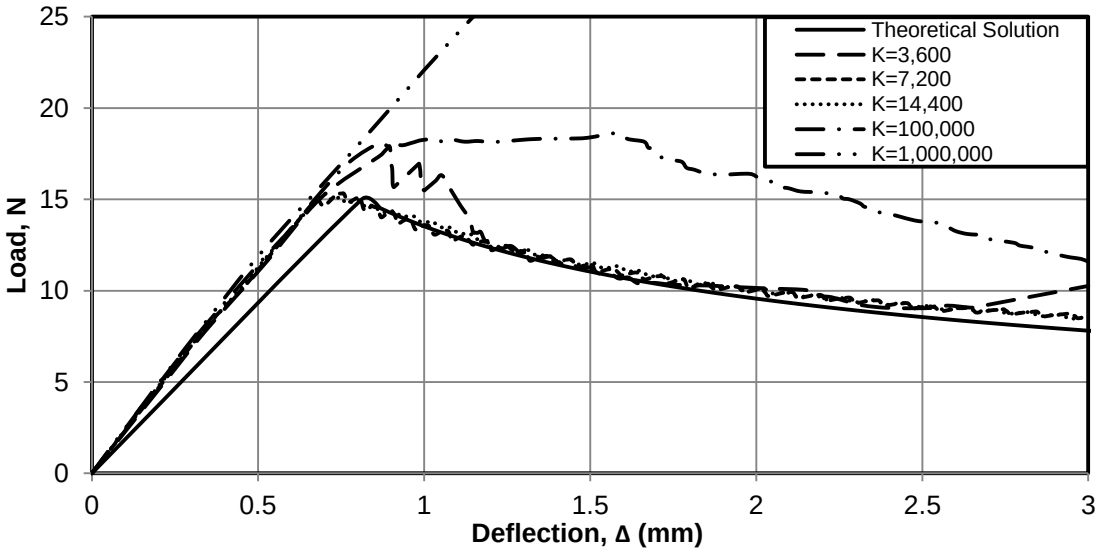


**Figure 10. Effect of penalty stiffness, $K$ (MPa/mm), on load-deflection curve for DCB (0.5 mm mesh, $N_e$ = 3, $\mu$ = 0.001)**

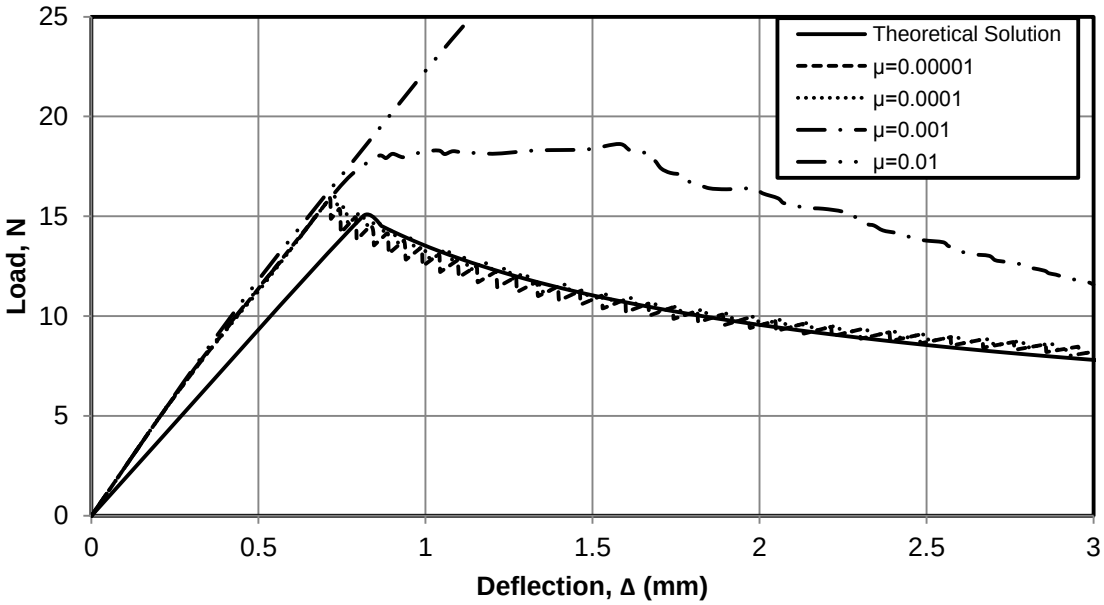


**Figure 11. Effect of viscosity, $\mu$, on load-deflection curve for DCB (0.5 mm mesh, $K$ = 100,000, $N_e$ = 3)**

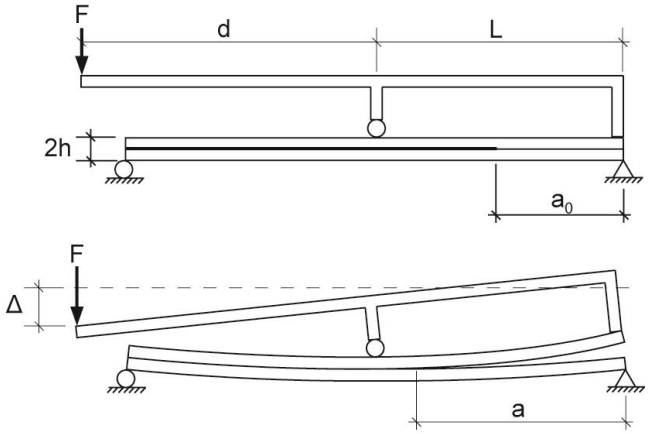


**Figure 12. MMB test setup**

***Mixed-Mode Bending Test***

Figure 12 provides the general configuration of the MMB test developed by Reeder and Crews [75]. The MMB validation tests used the material parameters provided in Table 2 and followed the experimental setup given in Song et al. [66]. The beam was 100 mm long total, 25.5 mm wide, with two 2.3 mm thick laminates and an initial crack length, $a_0$, of 27 mm. The length of the lever arm from the midpoint to the applied load ($d$) was 52.8 mm, which was chosen to correspond to a particular mode mixity ratio. Based on the equations from ASTM D6617 provided in Appendix A.3, the mode mixity used in Song et al. was 0.234. In each case, a mesh size of 0.5 mm was used as this was the most computationally effective and accurate mesh size studied in the DCB tests. The FEA used the same element types as in the DCB test; only the geometry and loading configuration of the beam were changed. The lever arm was represented as a rigid body that was tied to the beam at the midpoint with rotation allowed and tied to the beam at the pre-cracked end without rotation allowed.

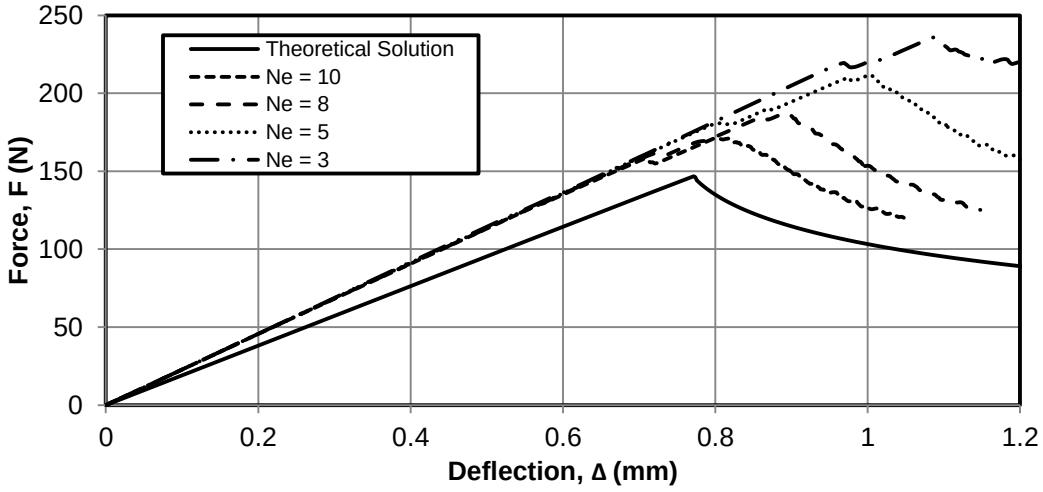


**Figure 13. Effect of interface strength on load-displacement curve for MMB ($K$ = 250,000, $\mu$ = 0.0001)**

The accuracy of the MMB test results was dependent on both the interface strength and the penalty stiffness as shown in Figure 13 and Figure 14. The results were much more sensitive to the value of $K$ than the DCB tests. As a result, $K$ generally had to be much higher than during the DCB tests, although too high a $K$ also resulted in inaccurate solutions. The number of elements in the cohesive zone also had to be much higher than in the DCB tests. Figure 14 depicts one possible combination for obtaining an accurate fit ($N_e$ = 8, $K$ = 660,000); other combinations of these two factors also yielded results close to the theoretical solution. In general, the approach to establishing these cohesive parameters was to select a reasonable mesh size, start with a relatively stiff $K$ as suggested in Eq. 24, and test variations of interface strength and $K$ values until achieving an accurate solution.

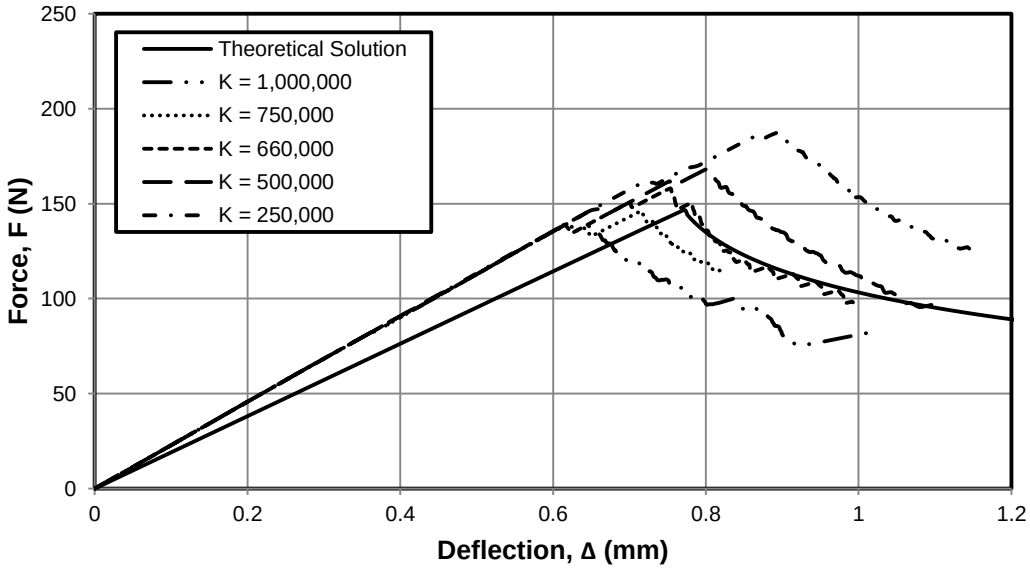


**Figure 14. Effect of penalty stiffness on load displacement curve for MMB ($N_e$ = 8, $\mu$ = 0.0001)**

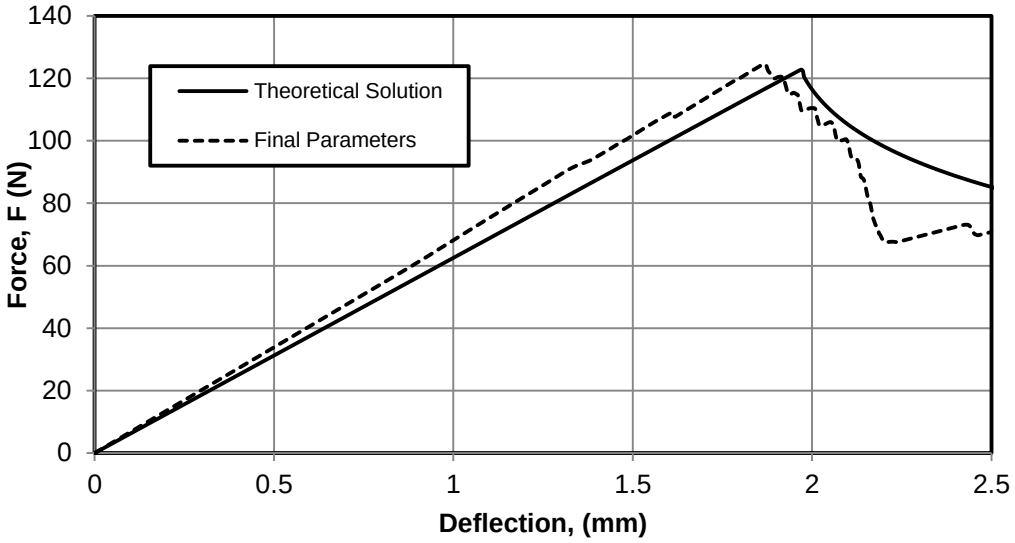


**Figure 15. MMB load-deflection curve for selected cohesive element parameters for E-glass/epoxy**

***Selection of Parameters***

Having established the validity of the general approach to calibrating cohesive parameters, the same tests were performed for an E-glass/epoxy composite to establish material properties for the composite impact tests. The FE results from the MMB test for these parameters (Figure 15), agree well with the theoretical solution on the initial portion for the load-deflection curve. The parameters of this test were identical to the previous MMB test, with the exception that $a_0$ was set to 35 mm in order to obtain better agreement between the initial elastic portion of the curve and the theoretical results. Table 3 provides the cohesive element properties used in Figure 15, while Table 1 provides the relevant lamina material properties. The large observed drop in force of the FE solution corresponded to the crack reaching and crossing mid-span of the MMB, after which the theoretical solution was no longer valid.

**Table 3. Cohesive element properties for E-glass/epoxy lamina**

| Property | Units | Value | Source |
|---|---|---|---|
| Mesh Size | mm | 0.5 | FEA |
| $T$ | MPa | 20 | FEA |
| $S$ | MPa | 50 | FEA |
| $K$ | MPa/mm | 500,000 | FEA |
| $\mu$ | - | 0.0001 | FEA |
| $G_{Ic}$ | N/mm | 0.118 | [8] |
| $G_{IIc}$ | N/mm | 2.905 | [8] |
| $\eta$ | - | 2.6 | [8] |

## 3.4 Low-Velocity Impact on Composite

The composite model was validated for low-velocity impact using data gathered by Evci and Gulgec [31]. The experimental setup chosen consisted of a unidirectional E-glass/epoxy plate composed of 9 layers of alternating 0° and 90° plies, 4.04 mm thick total and 100 mm x 100 mm square. This plate was subjected to a low-velocity impact with impact energy of 20 J by a 10 mm diameter hardened steel drop-weight in an Intron Dynatup 9250 instrumented test system. Circular clamps measuring approximately 40 mm in diameter held the specimens during testing. A comparison of numerical and experimental results for load vs. time and impact energy vs. time validated the model. A qualitative comparison of damage characteristics was also performed.

***Finite Element Model***

The finite element model consisted of 9 separate plies, each 0.44 mm thick, with a 0.01 mm thick cohesive layer sandwiched between each ply. Plies were modeled with SC8R: 8-node, quadrilateral, reduced integration, continuum shell elements, with enhanced hourglass control, a maximum degradation of 85%, and a Hashin damage viscous stabilization factor of $1 \times 10^{-7}$ in order to prevent excessive element distortion.

The ply material studied was E-glass/epoxy; the material properties were previously provided in Table 1. At the center of the mesh, elements are 0.5 mm x 0.5 mm; their size increased with distance from the impact zone in order to reduce computational demand (Figure 16). The interlaminar layers were modeled with COH3D8, 8-node cohesive elements, with a regular mesh of 0.5 mm x 0.5 mm, as determined by the interlaminar damage validation. Interlaminar layer properties were provided in Table 3. Maximum degradation for these elements was set at 99% and linear bulk viscosity was set at 0 as suggested in the Abaqus user manual [73]. These cohesive layers were tied to the ply layers using surface-to-surface ties.

The impactor was modeled as a rigid body with a mass of 2 kg with a velocity of 4.472 m/s, providing initial impact energy of 20 J. Contact between the impactor and composite layers, as well as contact between plies suffering delaminations, was modeled with a friction penalty of 0.65, based on friction between composite parts. The plate was given fixed boundary conditions along the bottom and top edges, representing the circular clamps, while the motion of the impactor was restricted to only the normal dimension.

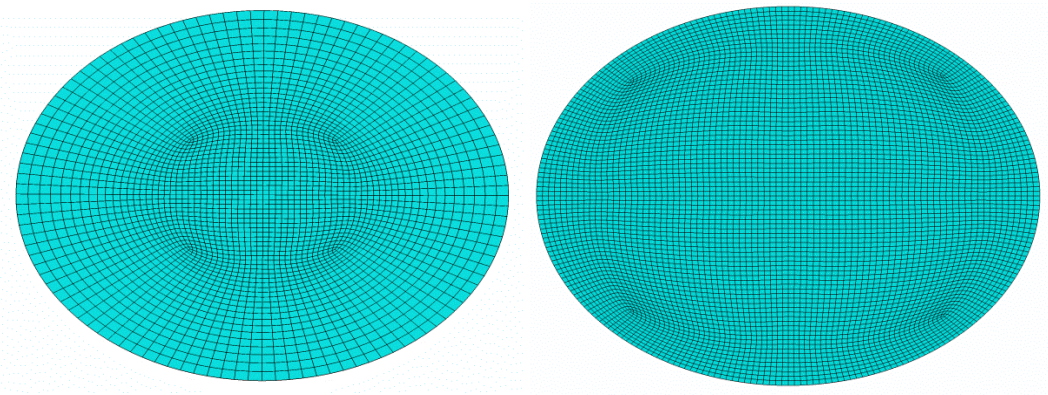

**Figure 16. Mesh for ply layers (left) and cohesive layers (right)**

The impact simulation was run in Abaqus/Explicit, with a time span of 0.005 seconds. The linear bulk viscosity parameter was set at the recommended value of 0.06, and the quadratic bulk viscosity parameter was the recommended value of 1.2 [73].

### *Validation Results*

A comparison of results from the FEA with experimental data showed good agreement between the two in terms of absorbed energy and contact force. Figure 17 graphs absorbed energy vs. time for numerical and experimental results. Acceleration due to gravity was not modeled; the additional energy related to the conversion of potential energy due to the change in position of the impactor and composite during deflection was neglected. This assumption explained the higher level of total energy seen in the experimental data in Figure 17. Factors which might have led to higher final levels of absorbed energy included delamination in the composite beyond the clamped section, which was not modeled, and vibrations in the testing apparatus.

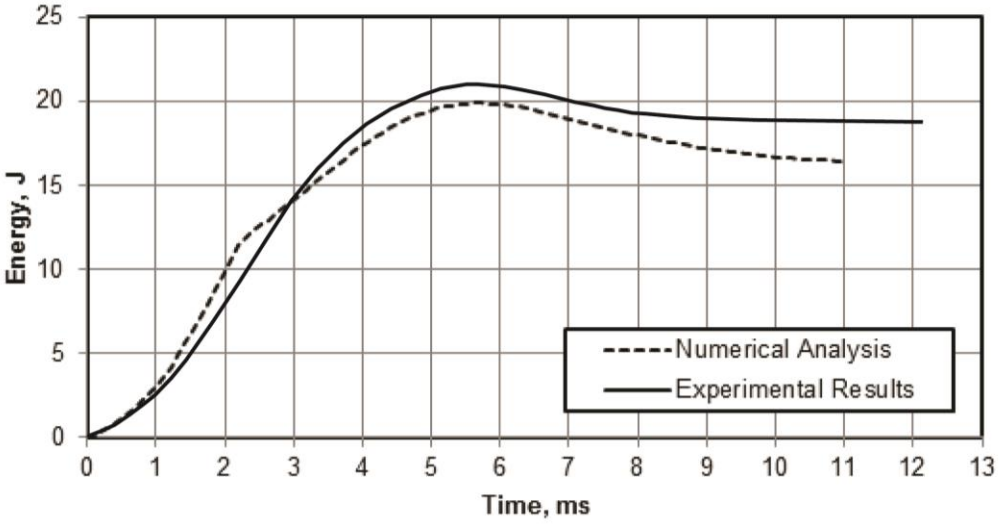


**Figure 17. Comparison of absorbed energy for validation (20 J)**

Figure 18 compares the contact force in the FEA and experimental data. The Hertzian force, corresponding to the first onset of delamination, was experimentally determined to be 1370.5 N; FEA gave a result of 1725.7 N. The maximum contact force, measured at 5170.4 N, was predicted by FEA to be 5602.9 N. A major difference in the graphs of the contact force was the much larger drop after maximum contact force during numerical analysis. This behavior corresponded to massive intralaminar damage occurring at this time. Similar drops were reported in other experiments on low-velocity impacts on composites, such as in González et al. [41].

Qualitatively, damage progression followed expected patterns. Delaminations (Figure 19) took the expected peanut shape and changed alignment with the alternating directions of the bordering plies, while increasing in size from top to bottom. Figure 20, a section cut, shows the delamination and ply separation at the middle of the specimen at Time = 11 ms; ply compression failure and buckling were observed at the top ply, while the bottom ply split due to tension failure owing to bending stresses.

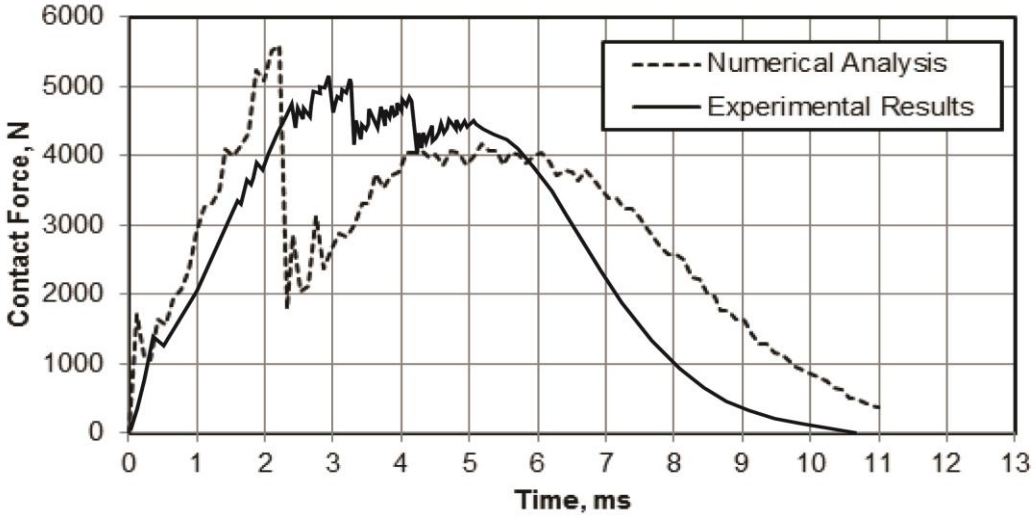


**Figure 18. Comparison of contact force for validation – 20 J**

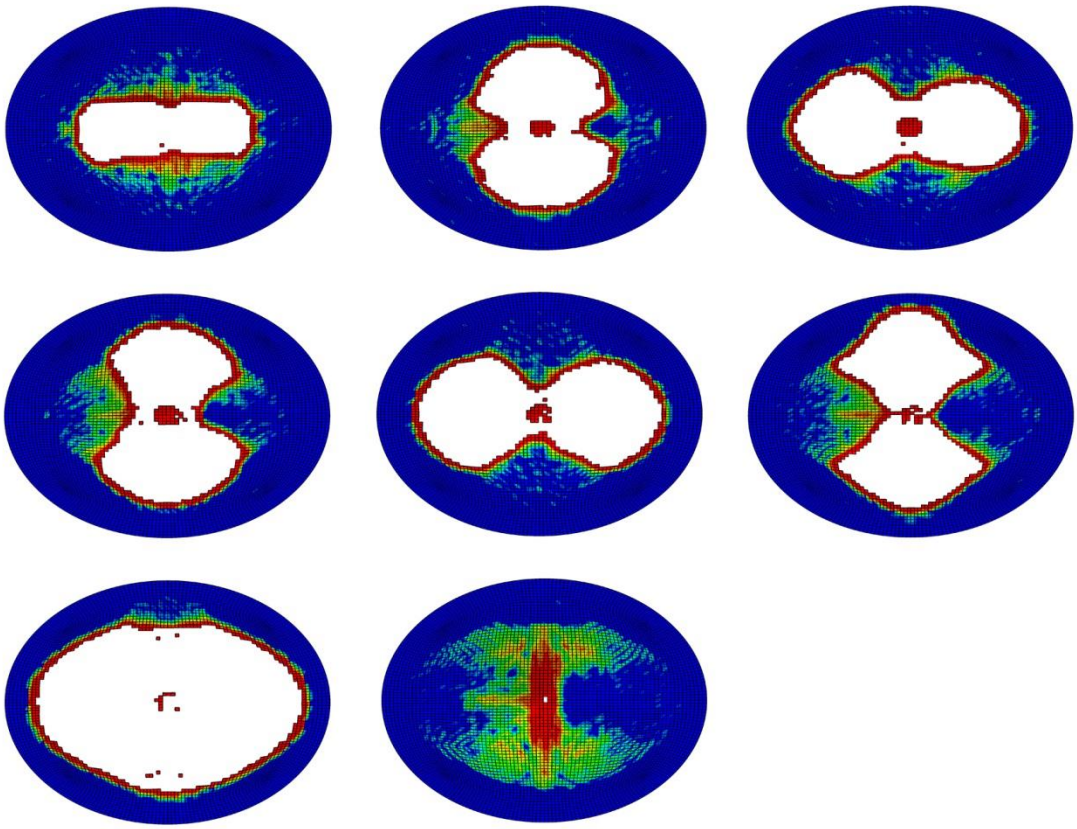

**Figure 19. Delamination in cohesive layers from top (top right) to bottom (bottom middle) at time = 0.88 ms**

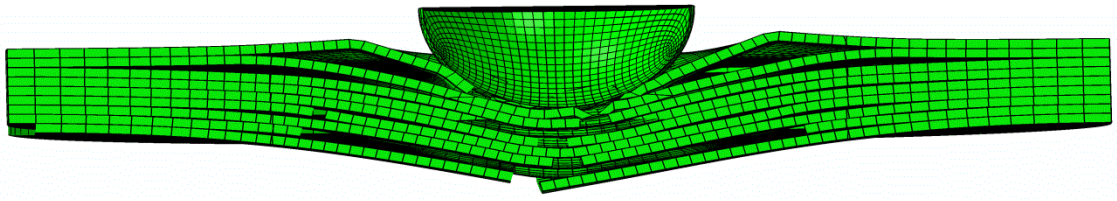

**Figure 20. Delamination and ply damage in composite at time = 11 ms**

## 3.5 Adhesive Layer Damage Model

***Selection of Damage Model***

The epoxy adhesive bonding composite to metal was modeled using CZM traction-separation laws, similar to those used for delamination. For the adhesive, the thickness (0.2 mm) was not negligible, and it was incorporated into the model through a more precise definition of the stiffness, $K$. The stiffness is defined as the corresponding Young's or shear modulus divided by the thickness of the adhesive layer ($T_c$) such that $K_n = E/T_c$ and $K_s = G_{12}/T_c$, and it is governed by the relationship $\mathbf{t} = \mathbf{K\varepsilon}$ [76]. As in delamination modeling, Mode III is assumed to be equal to Mode II. Experiments suggest that the greater the adhesive thickness, the higher the apparent critical fracture energy [77]. This fact leads to disparate reporting of the critical fracture energy for the same material, especially when considering $G_{IIc}$. Araldite 2015, the adhesive used in this validation, was variously reported to have a $G_{IIc}$ of 2.1 N/mm [78] or 4.7 N/mm [76, 79] for 0.2 mm thick adhesive, up to 11.3 N/mm for 0.5 mm thickness and 21.2 for 1 mm thickness [80].

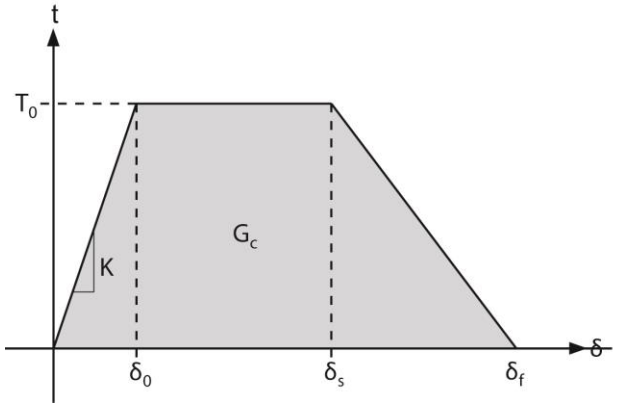


**Figure 21. Trapezoidal traction-separation law**

A second difference between modeling delamination and adhesive failure is the dependence of behavior on the shape of the governing traction-separation curve. For brittle adhesives the choice of curve shape typically matters very little; a standard bi-linear curve suffices. However, for ductile adhesives, a trapezoidal law (Figure 21) often better captures correct traction-separation behavior. Campilho et al. suggested defining this trapezoidal shape by setting $\delta_s$ equal to 0.8 of $\delta_f$. The damage variable, $D$, is still defined as in Equations 34-36, with the value manipulated in order to represent the trapezoidal shape:

$$\text{for } \delta_0 \leq \delta_{max} < \delta_s, \qquad D = \frac{\delta_{max} - \delta_0}{\delta_{max}} \tag{41}$$

$$\text{for } \delta_{max} \geq \delta_s, \qquad D = \frac{\delta_0\left(\delta_{max} - \delta_f\right)}{\delta_{max}\left(\delta_f - \delta_s\right)} + 1 \tag{42}$$

Due to difficulties associated with inputting a mixed-mode trapezoidal traction-separation curve into Abaqus, the linear form of the power law was used as in Campilho et al. [76]:

$$\frac{G_I}{G_{Ic}} + \frac{G_{II}}{G_{IIc}} = 1 \tag{43}$$

***Validation Results***

Araldite 2015, a ductile epoxy adhesive, was modeled to validate both the adhesive model and the complete hybrid composite. In both adhesive validation tests and in the hybrid structure the thickness of the adhesive bond was 0.2 mm. Material properties used in the analysis are provided in Table 4.

**Table 4. Material Properties for 0.2 mm thick Araldite 2015 adhesive**

| Property | Units | Value | Source |
|---|---|---|---|
| $\rho$ | g/cc | 1.9 | [76] |
| $E_1$ | GPa | 1.85 | [76] |
| $\nu_{12}$ | - | 0.33 | [76] |
| $G_{12}$ | GPa | 0.487 | [78] |
| $\sigma_{tf} = T_0$ | MPa | 21.63 | [76] |
| $\varepsilon_f$ | % | 4.77 | [76] |
| $\tau_f = S_0$ | MPa | 17.9 | [78] |
| $\gamma_f$ | % | 43.9 | [76] |
| $G_{Ic}$ | N/mm | 0.43 | [76] |
| $G_{IIc}$ | N/mm | 2.1 | [78] |

Validation of Mode I behavior was performed using the DCB setup (Figure 8) tested in da Silva et al. [78]. This setup employed 12.7 mm thick steel adherends, 280 mm long (from load application to beam end) and 25 mm wide, bonded together with 0.2 mm Araldite 2015 epoxy adhesive. The initial crack length was set at 50 mm. The adhesive was modeled using a 0.5 mm x 0.5 mm cohesive mesh, with thickness accounted for numerically by the calculation of *K*. Figure 22 shows a DCB load-deflection curve comparing bi-linear and trapezoidal traction-separation curve FEA results to experimental data. These results showed good agreement in both level of load required to initiate cracking and level of load required to sustain constant crack growth, for both trapezoidal and bi-linear curves. The initial slope of the load-deflection curve is only dependent on the initial crack length and the elastic properties of the adherends; thus, the 0.5 mm difference between deflection at the peak load in FE and deflection at the peak load in the experimental results must be due to a misreporting of factors or measurement error.

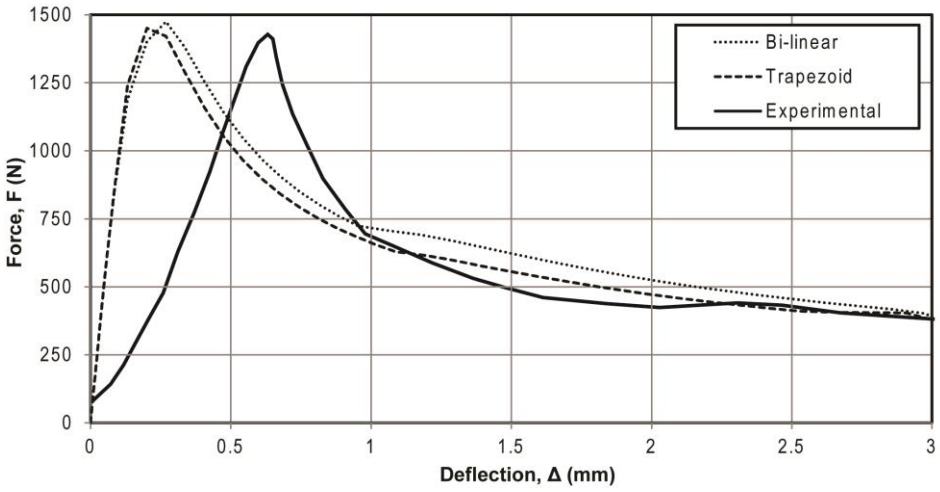


**Figure 22. DCB load-deflection curve for adhesive validation**

Validation of Mode II was performed using an end-notched flexure (ENF) test, which as configured as shown in Figure 23 and tested against experimental data in da Silva et al. [80]. The ENF test consists of applying a load to the mid-span of a simply-supported beam consisting of two adherends bonded together with an adhesive. An initial crack, $a_0$, is present on one side of the beam; it propagates towards mid-span in Mode II during flexural loading. This specific ENF test consisted of 12.7 mm steel adherends, 270 mm long between supports and 25 mm wide, with a 0.2 mm thick Araldite 2015 adhesive and a 50 mm initial crack length. As in the DCB, the finite element analysis consisted of a 0.5 mm x 0.5 mm cohesive element mesh. The two previously mentioned values of $G_{IIc}$ were each tested with both bi-linear and trapezoidal curves.

Figure 24 shows that the $G_{IIc}$ of 2.1 N/mm measured in the validation experiment provided a more accurate estimation of force for crack initiation and propagation than the 4.7 N/mm measured in Camphilo et al [76]. The trapezoidal curve predicted the

maximum force more accurately than the bi-linear curve. Based on these results, the proposed model for Araldite 2015 consisted of a bi-linear traction-separation curve for Mode I and a trapezoidal curve for Mode II, with mixed mode behavior governed by a linear power law (Eq. 43).

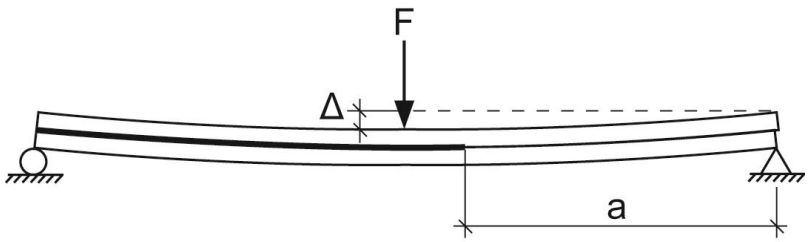


**Figure 23. ENF test setup**

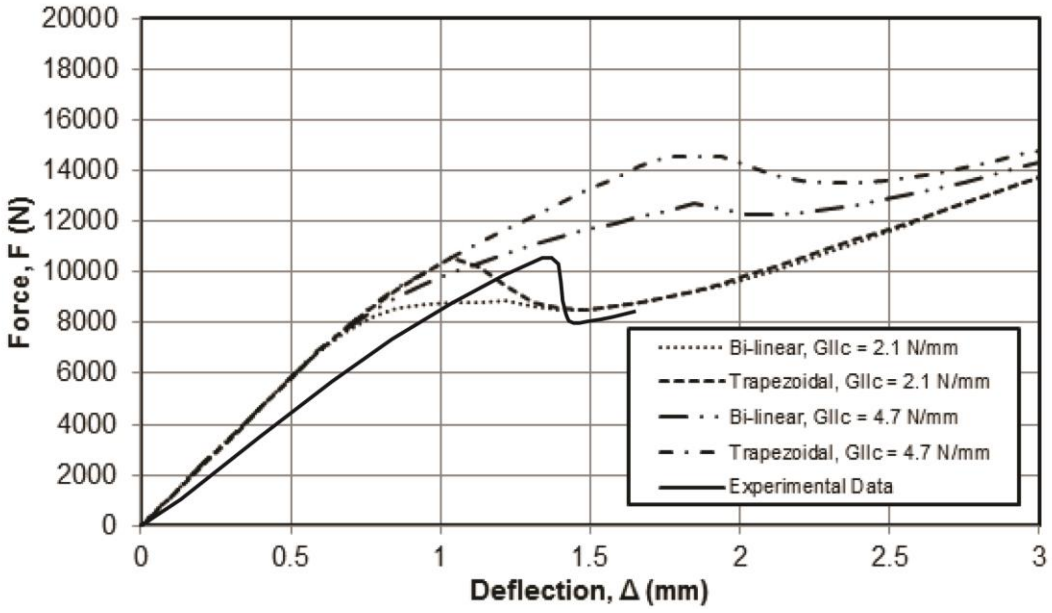


**Figure 24. ENF load-deflection curve for adhesive validation**

## 3.6 Metal Damage Model

***Selection of Damage Model***

The requirements for a material model for the steel substrate were that it must accurately predict the following: maximum deflection, final plastic deformation, and any damage incurred. Under an impact, strain rate effects on material behavior also had to be considered. The Johnson-Cook model for metal plasticity and damage, which is widely used for impact analysis in metals [54, 81, 82] and fully implemented within the ABAQUS code, was chosen to represent this behavior. The Johnson-Cook plasticity model was designed to account for large strains, high strain rates, and high temperatures. The equation gives the Mises tensile flow stress, $\sigma$, as:

$$\sigma = (A + B\varepsilon^n)(1 + C\ln\frac{\dot{\varepsilon}}{\dot{\varepsilon}_0})(1 - T^m) \tag{44}$$

In this equation, $\dot{\varepsilon}$ / $\dot{\varepsilon}_0$ is the plastic strain rate for $\dot{\varepsilon}_0 = 1\ \mathrm{s}^{-1}$, $T$ is the homologous temperature, $\boldsymbol{\varepsilon}$ is the equivalent plastic strain, and $A, B, C, n$, and $m$ are material constants derived experimentally. The first section of the equation gives the stress as a function of strain without considering strain rate or temperature, the second section represents the effects of strain rate, and the third section represents the effects of temperature [10]. The temperature was not expected to have an effect on performance in these tests.

In addition to the plasticity model, the Johnson Cook fracture model may also be incorporated if needed. This model is governed by:

$$\varepsilon^f = \left(D_1 + D_2 e^{D_3\sigma^*}\right)\left(1 + D_4 \ln\frac{\dot{\varepsilon}}{\dot{\varepsilon}_0}\right)(1 + D_5 T) \tag{45}$$

In Equation 45, $\dot{\varepsilon}$ / $\dot{\varepsilon}_0$ and $T$ are the same as in the plasticity model, $D_1$ through $D_5$ are material constants determined experimentally, $\varepsilon^f$ is the strain at fracture, and $\sigma^* = \sigma_m/\bar{\sigma}$

($\sigma_m$ is average of the three normal stresses, and $\bar{\sigma}$ is the von Mises equivalent stress) [10]. For low-energy impact velocities, the damage model is unnecessary as shown in the following validation study. However, as impact energy nears the ballistic limit, this damage equation is necessary to fully capture the metal behavior.

### *Validation Results*

Since no experimental data for low-velocity impacts on thin stainless steel sheets was found in the literature review, validation was instead performed on aluminum sheets using the Johnson-Cook damage model. Experimental data obtained by Mohotti et al. [81] was used for validation. The experimental setup consisted of a 300 mm x 300 mm AA5083-H116 aluminum plate of 3 mm thickness, which was impacted at 9.02 m/s by a 5 kg, 37 mm diameter cylinder at its center. Relevant material properties for AA5083-H116 aluminum are provided in Table 5.

**Table 5. Material properties for AA5083-H116 aluminum**

| Property | Units | Value | Source |
|---|---|---|---|
| $E$ | GPa | 70 | [83] |
| $\nu$ | - | 0.33 | [83] |
| $\rho$ | g/cc | 2.66 | [83] |
| $A$ | MPa | 215 | [81] |
| $B$ | MPa | 280 | [83] |
| $n$ | - | 0.404 | [83] |
| $C$ | - | 0.0085 | [83] |
| Ref. Strain Rate | $s^{-1}$ | 0.001 | [83] |
| $D_1$ | - | 0.178 | [81] |
| $D_2$ | - | 0.389 | [81] |
| $D_3$ | - | -2.25 | [81] |
| $D_4$ | - | 0.147 | [81] |
| $D_5$ | - | 16.8 | [81] |

The finite element model of the aluminum plate consisted of C3D8R, 8-node, reduced integration, continuum solid elements. At the center of the plate, where damage was expected, the mesh was sized at approximately 0.5 mm x 0.5 mm with three 1 mm deep elements through-thickness in order to maintain an acceptable aspect ratio. The mesh size was enlarged with increasing distance from the center. The impactor was represented as a rigid body. Contact was modeled as tangential with a friction coefficient of 0.61.

The deflection-time curves for this impact are provided in Figure 25; result values are compared in Table 6. Permanent deflection in the FEA was calculated as the average deflection during the oscillations seen in Figure 25. While predicted permanent deflection was off by 11.6% compared to 7.4% for maximum deflection, the difference in deformations between the experimental and FEA results was the same for both permanent and maximum deflection at about 1.4 mm. The differences seen in the unloading portion of Figure 25 were due at least in part to the absence of damping in the FEA.

Figure 26 shows the residual stress caused by permanent plastic deformation of the aluminum plate after impact. Figure 27 shows the shape of the deformation and state of stress just before rebound.

**Table 6. Comparison of deflections from FE and laboratory data**

| Data Source | Max. Deformation (mm) | Percent Difference (%) | Permanent Deformation (mm) | Percent Difference (%) |
|---|---|---|---|---|
| Experimental | 18.3 | - | 12.8 | - |
| FEA | 17.0 | 7.37 | 11.4 | 11.57 |

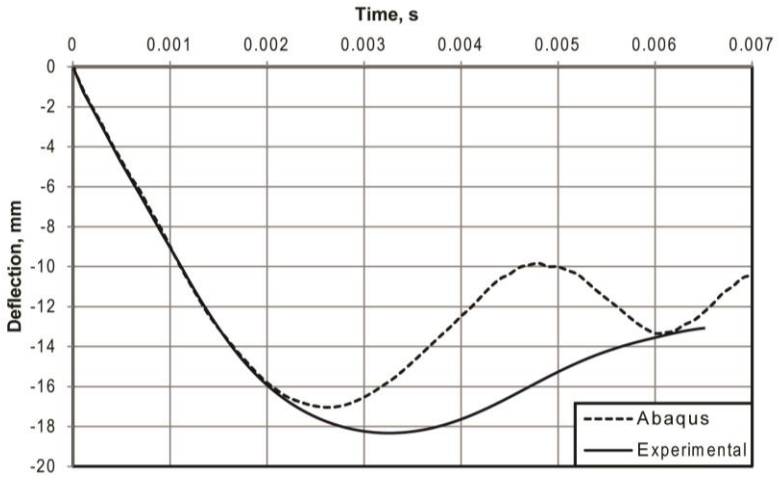


**Figure 25. Comparison of FEM and experimental time history deflections for aluminum impact**

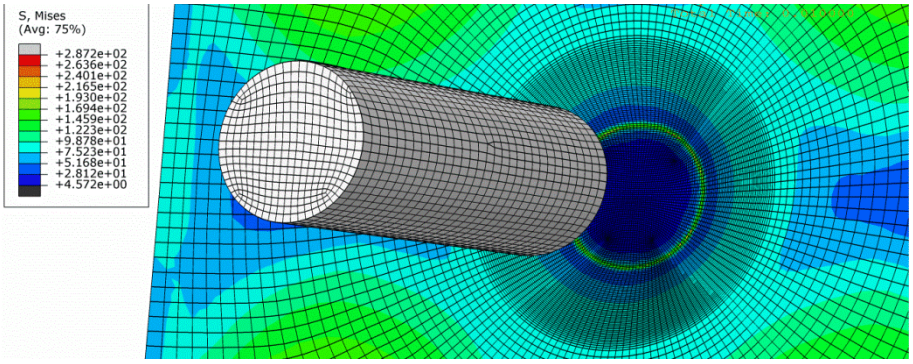


**Figure 26. Residual stresses at areas of plastic deformation**

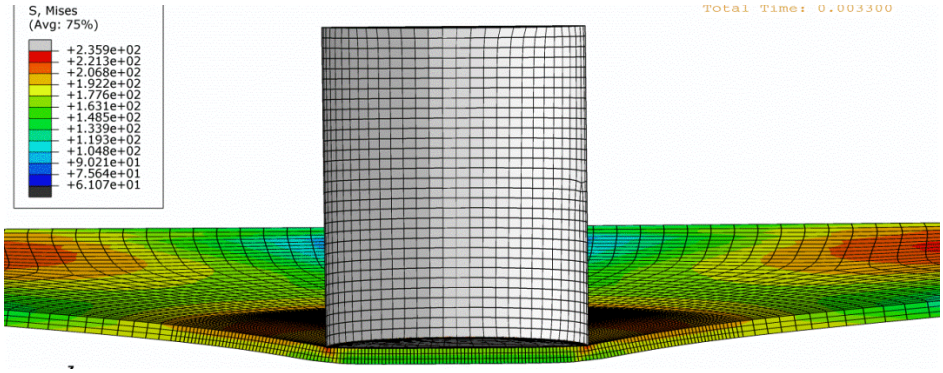


**Figure 27. Stresses at maximum deformation during impact**

# CHAPTER IV

# HYBRID MODEL VALIDATION

## 4.1 Material Properties

The limited availability of experimental data concerning low-velocity impact on composite patches, required for validation of the finite element modeling approach, controlled the selection of materials and validation configuration. Akimoto et al. [52] conducted a series of low-velocity impact experiments on unidirectional E-glass/polyester composites bonded to SUS304 stainless steel plates with Araldite 2015 epoxy adhesive (Figure 28). These experiments formed the basis of the validation presented in this chapter.

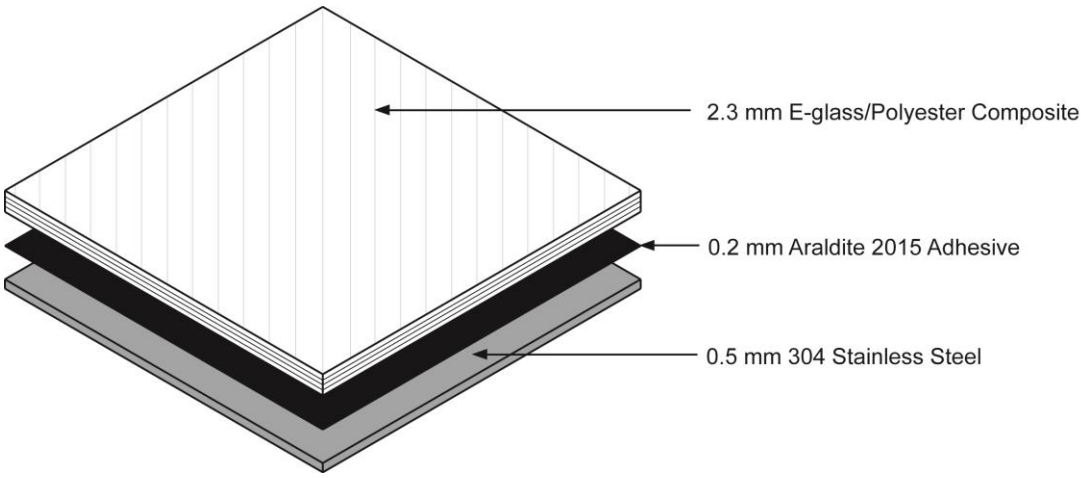


**Figure 28. Hybrid composite configuration for Akimoto et al.**

***Composite Properties***

The composite, consisting of E-glass fibers and a Scott Bader Crystic 272 polyester matrix, had an unusually low fiber volume ratio ($V_f$) of 30%, whereas a value of 50-60% is more typical for lamina material properties found in the literature. Thus, elastic and strength material properties of the lamina had to be calculated from the constitutive properties. The E-glass fiber properties are provided in Table 7, and the polyester matrix properties are provided in Table 8.

The resulting lamina properties used in the hybrid validation case are provided in Table 9. Appendix A.1 provides the formulas employed to determine the elastic and strength properties in Table 9 from the properties provided in Table 7 and Table 8. Due to a lack of a theoretical method for approximating the energy dissipation rates as well as experimental data for these variables, the energy dissipation rate values had to be assumed. Values of $G_f{}^t$ = $G_f{}^c$ = 15 and $G_m{}^t$ = $G_m{}^c$ = 1are based on the assumptions made in Lapczyk & Hurtado [5]. Using the properties in Table 9, new cohesive element parameters were determined through the methods described in Section 3.3. Results from this calibration are provided in Table 10.

**Table 7. Material properties for E-glass fibers**

| Property | Units | Value | Source |
|---|---|---|---|
| $V_f$ | % | 30 | - |
| $E_{1f}$ | GPa | 74 | [62] |
| $E_{2f}$ | GPa | 74 | [62] |
| $\nu_{12f}$ | - | 0.2 | [62] |
| $G_{12f}$ | GPa | 30.8 | [62] |
| $G_{23f}$ | GPa | 30.8 | [62] |
| $X_{tf}$ | MPa | 2150 | [62] |
| $X_{cf}$ | MPa | 1450 | [62] |
| $\varepsilon_{1Tf}$ | % | 2.905 | [62] |
| $\varepsilon_{1Cf}$ | % | 1.959 | [62] |

**Table 8. Material properties for Scott Bader Crystic 272 matrix**

| Property | Units | Value | Source |
|---|---|---|---|
| $V_m$ | % | 70 | - |
| $E_m$ | GPa | 3.5 | [84] |
| $\nu_m$ | - | 0.33 | [85] |
| $G_m$ | GPa | 1.32 | - |
| $Y_{tm}$ | MPa | 62.4 | [84] |
| $Y_{cm}$ | MPa | 127.5 | [84] |
| $S_{Lm}$ | MPa | 45 | [86] |
| $\varepsilon_{2Tm}$ | % | 2.3 | [84] |

**Table 9. Calculated material properties for E-glass/polyester composite**

| Property | Units | Value |
|---|---|---|
| $\rho$ | g/cc | |
| $E_1$ | GPa | 24.650 |
| $E_2$ | GPa | 6.127 |
| $E_3$ | GPa | 6.127 |
| $\nu_{12}$ | - | 0.291 |
| $\nu_{13}$ | - | 0.291 |
| $\nu_{23}$ | - | 0.433 |
| $G_{12}$ | GPa | 2.316 |
| $G_{13}$ | GPa | 2.316 |
| $G_{23}$ | GPa | 2.132 |
| $X_t$ | MPa | 716.182 |
| $X_c$ | MPa | 416.646 |
| $Y_t$ | MPa | 41.244 |
| $Y_c$ | MPa | 84.272 |
| $S_L$ | MPa | 29.699 |
| $S_T$ | MPa | 31.752 |

**Table 10. Cohesive element properties for E-glass/polyester**

| Property | Units | Value | Source |
|---|---|---|---|
| Mesh Size | mm | 0.5 | FEA |
| $T$ | Mpa | 41.2 | FEA |
| $S$ | MPa | 29.7 | FEA |
| $K$ | MPa/mm | 80,000 | FEA |
| $G_{Ic}$ | N/mm | 1.1 | [87] |
| $G_{IIc}$ | N/mm | 2.8 | [87] |
| $\eta$ | - | 2.6 | assumed |

**Table 11. Material properties for SUS304 stainless steel**

| Property | Units | Value | Source |
|---|---|---|---|
| $E$ | GPa | 193 | [88] |
| $G$ | GPa | 78 | [88] |
| $\nu$ | - | 0.3 | [88] |
| $\rho$ | g/cc | 8.03 | [88] |
| $A$ | MPa | 545 | [82] |
| $B$ | MPa | 1571 | [82] |
| $n$ | - | 0.867 | [82] |
| $C$ | - | 0.01043 | [82] |
| Ref. Strain Rate | $s^{-1}$ | $10^{-3}$ | [82] |

***Metal and Adhesive Material Properties***

The metal substrate was composed of 0.5 mm thick SUS304 steel, a common grade of stainless steel. Material properties for the steel are provided in Table 11, including values for the elastic behavior and Johnson-Cook plastic deformation. The material properties for Araldite 2015 were previously provided in Table 4.

## 4.2 Experimental and FEA Setup

As seen in Figure 28, the experimental setup consisted of a 60 mm x 60 mm hybrid plate, struck by a 20 mm DIA, 1.91 kg hemispherical impactor at 3.5 m/s. Four plies, arranged quasi-axially as [0,-45, 90, +45] with a fiber volume fraction of 30%, composed the 2.3 mm thick E-glass/polyester composite layer. The 0.2 mm thick Araldite 2015 adhesive bonded this composite to the undamaged 0.5 mm thick SUS304 stainless steel sheet.

Each composite ply was modeled with SC8R solid, 8-node, reduced integration, hexagonal continuum shell elements, in order to apply the Hashin failure criteria. Elements were given enhanced hourglass distortion control to prevent flattening of plies

in compression and excessive element distortion. Each ply was modeled with a single through-thickness element. Each element measured 0.5 mm x 0.5 mm x 0.5675 mm thick.

The three intralaminar layers and the adhesive layer were modeled with COH3D8, 8-node, hexagonal cohesive elements. Element deletion was allowed in order to simulate delamination; maximum element degradation was set at 99%. Each of cohesive layers was 0.01 mm thick and meshed with elements, sized 0.5 mm x 0.5 mm, while the adhesive layer was 0.2 mm thick with 0.5 x 0.5 mm sized elements. In order to increase the stable time increment, the density of the cohesive elements was increased from 1.9 $e^{-9}$ to 1.7 $e^{-7}$ tonnes/$mm^3$, which had the effect of increasing the overall model mass by only about 10% due to the small volume of these elements. These layers were connected to the neighboring ply or steel layers by surface-to-surface tie constraints. Contact between plies post-delamination was modeled with general contact (tangential behavior with a penalty friction coefficient of 0.65, which was based on composite on composite friction).

The steel layer was modeled with 0.5 mm x 0.5 mm x0.5 mm C3D8R, 8-node, reduced integration, solid continuum elements. The impactor was modeled as a discrete rigid body for computational efficiency. This rigid body was tied to a reference node upon which the mass, velocity, and initial boundary conditions were placed. The impactor was restrained from movement in the 1 and 2 directions, and all rotation was prevented in order to replicate the test conditions. The model ran in Abaqus/Explicit for 4 ms; the linear bulk viscosity parameter was set at the recommended value of 0.06, and the quadratic bulk viscosity parameter was the recommended value of 1.2 [73].

## 4.3 Validation Results

The load-deflection curve for this analysis is provided in Figure 29. Table 12 compares the percent differences between the FEA results and the experimental data. Good agreement was found between the FEA results and experimental test data concerning energy absorption, with predicted energy absorption only 6.6% lower than experimental data. The numerical simulation predicted a deflection of 0.55 mm greater than experimental results showed, but it predicted a much lower maximum contact force. These results indicate that the finite element model experienced a greater loss of stiffness due to damage than that seen in the experimental results, especially after about 1 mm deflection. This discrepancy is not unexpected given the number of assumptions made to create the validation model.

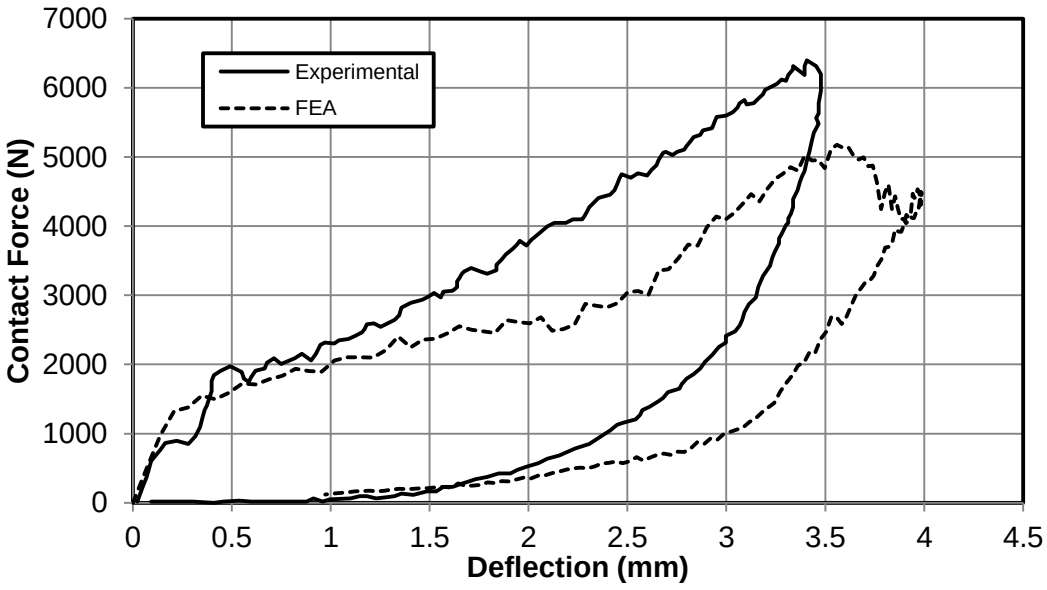


**Figure 29. Load-deflection for hybrid composite validation**

**Table 12. Comparison of FEA results to experimental data**

| Data Type | Maximum Deflection (mm) | Percent Difference (%) | Maximum Contact Force (N) | Percent Difference (%) | Energy Absorbed (J) | Percent Difference (%) |
|---|---|---|---|---|---|---|
| Experimental | 3.44 | - | 6350 | - | 8.88 | - |
| FEA | 3.986 | 14.71 | 5178 | 20.33 | 8.32 | 6.56 |

The slope of the load-deflection curve shown in Figure 29 changed drastically at a deflection of about 2.5 mm, which corresponded to a time around 0.8 ms. Looking at the contact force history graph (Figure 30), this slope change corresponded to a substantial increase in loading rate up to the point of maximum contact force. Prior to this point, delaminations grew slowly and were confined to the area around the impact site. After this point, delaminations expanded rapidly, especially between the third and fourth plies. At a time of 1.3 ms, the first ply failure occurred on the top ply, resulting in a reduction of contact force similar but less drastic than that seen in Figure 18 in the composite impact validation. After this, ply damage and plastic deformation of the metal were the primary damage modes as the contact force oscillated around 4,500 N until rebounding began. This behavior was consistent with that seen in Figure 18. The Hertzian failure point, corresponding to the first delamination, was much less pronounced in the hybrid than in the composite alone; Hertzian failure corresponded to a change in slope rather than a significant drop in force. Overall, the oscillations and drops seen in the force history graph for the hybrid composite were less pronounced than those in the composite alone. This smoothing effect was likely due to the energy absorption of the plastic deformation of the metal.

Figure 31 serves as a point of comparison to Figure 17 from the composite validation. Note the similar shapes of the energy-time curves; the larger span of the hybrid composite validation sample allowed for more elastic strain energy to be stored and released, hence the lower percentage of absorbed energy.

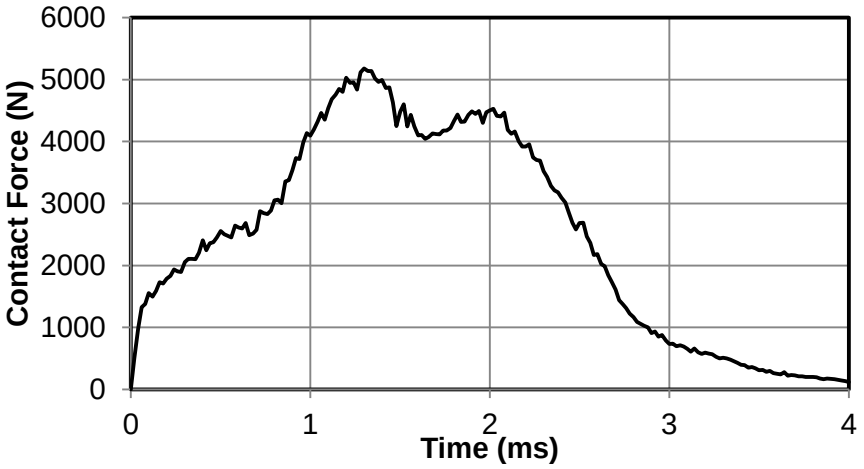


**Figure 30. Contact force – time curve for FEA**

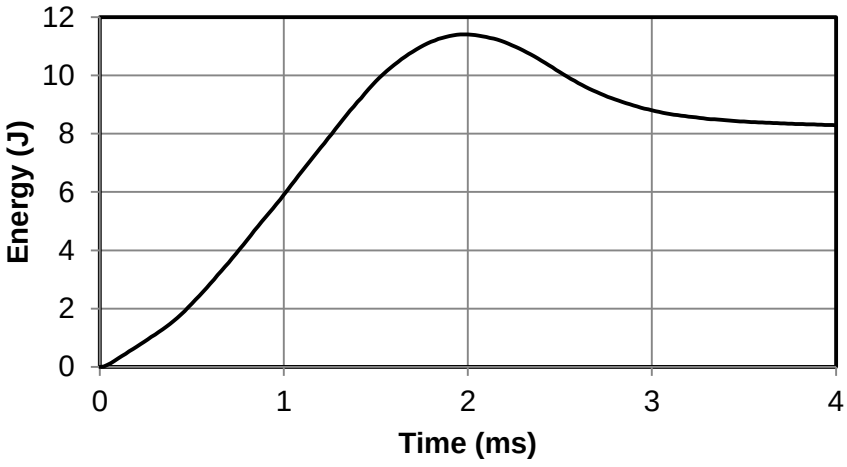


**Figure 31. Energy-time curve for FEA**

The delaminations observed in the hybrid composite (Figure 32) increased in size with depth and took the expected peanut shape, which was distorted by the closer orientation of the neighboring plies (45° difference between plies rather than 90°). Figure 33 shows the adhesive's final state. Mode II shear damage during loading caused most of the adhesive damage; however, the composite pulling away from the plastically deformed steel in Mode I during rebound caused the complete disbond at the site of impact. Figure 34, a section through the model, shows the adhesive intact at maximum deflection. It is then pulled apart by the end of the analysis. Most composite plies returned to their approximate original positions, except the fourth layer, which was still mostly adhered to the deformed steel.

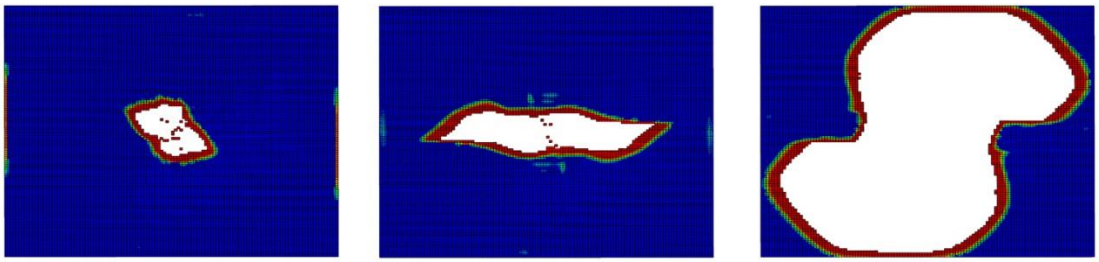

**Figure 32. Delamination between ply 1 and 2 (left), 2 and 3 (middle), 3 and 4 (right) at time = 4 ms**

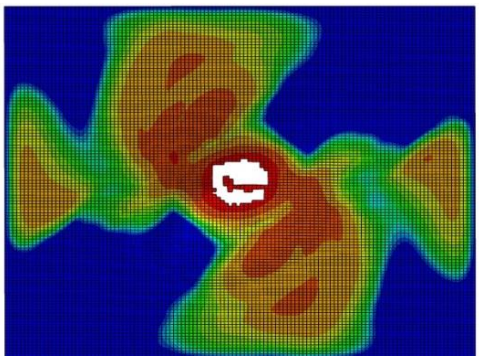

**Figure 33. Adhesive damage in validation FEA at time = 4 ms**

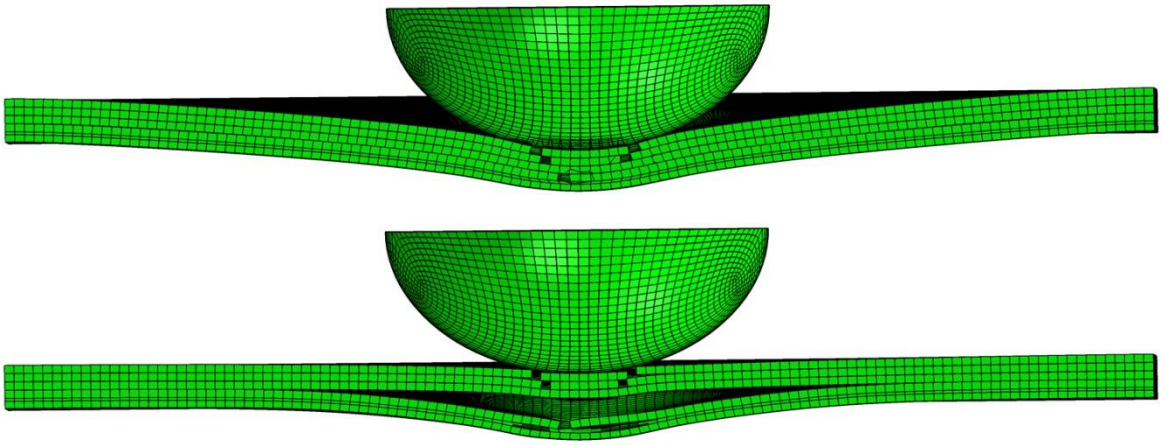

**Figure 34. Section through middle of plate at maximum deflection (top) and time = 4 ms (bottom)**

# CHAPTER V

# SENSITIVITY STUDY

## 5.1 Parameters Studied

The sensitivity study was conducted to determine the effect of uncertain inputs on the performance of the hybrid composite model. The uncertainties explored in the study included the following: the mesh sensitivity, impactor model, composite strength (represented as fiber volume ratio), ply thickness, and steel Johnson-Cook material properties. The model from Chapter 4 was modified by changing each of these parameters only. Results were compared to the original model and to the experimental data.

## 5.2 Fiber Volume Ratio

The fiber volume percentage of the experimental composite was reported by Akimoto et al. to be 30%. However, as previously described, the lamina material properties were derived from theoretical and empirical formulas using constitutive properties. They were not verified by experimental measurements. Hence, considerable uncertainty existed in these values. Fiber volume was chosen as a way to vary the properties of the composite lamina. The longitudinal strength was of particular interest due to its predicted influence on the impact resistance of the composite [27]. To explore the effects of altering the fiber volume ratio ($V_f$) was varied from 0.3 to 0.6. Table 13 provides the material properties for each value of $V_f$ derived from the equations presented in Appendix A.1. Changing these properties was assumed to have no effect

on cohesive element properties. Since cohesive element properties were based primarily on the transverse tensile strength ($Y_t$) and shear strength ($S_L$), and these properties changed very little with increasing fiber volumes, this assumption was reasonable. The critical fracture energy associated with the cohesive elements could change due to fiber bridging, but more experimental data is needed to clarify this effect. The energy release rates for the lamina were not altered.

Results from these simulations are provided in Table 14. The load-deflection curves reflecting each of these values of $V_f$ are provided in Figure 35. Maximum deflection was most sensitive to $V_f$, registering a 8% decrease in deflection with an increase from 0.3 to 0.6 fiber volume content. The contact force was insensitive to the fiber volume ratio, while the energy absorbed only registered slight changes.

**Table 13. Material Properties for E-glass/polyester composite with varying fiber volume ratios**

| Property | Units | $V_f$ = 0.3 | $V_f$ = 0.4 | $V_f$ = 0.5 | $V_f$ = 0.6 |
|---|---|---|---|---|---|
| $E_1$ | GPa | 24.650 | 32.050 | 39.450 | 46.850 |
| $E_2$ | GPa | 6.127 | 6.546 | 6.960 | 7.369 |
| $E_3$ | GPa | 6.127 | 6.546 | 6.960 | 7.369 |
| $\nu_{12}$ | - | 0.291 | 0.311 | 0.331 | 0.351 |
| $\nu_{13}$ | - | 0.291 | 0.311 | 0.331 | 0.351 |
| $\nu_{23}$ | - | 0.433 | 0.427 | 0.419 | 0.408 |
| $G_{12}$ | GPa | 2.316 | 2.476 | 2.635 | 2.791 |
| $G_{13}$ | GPa | 2.316 | 2.476 | 2.635 | 2.791 |
| $G_{23}$ | GPa | 2.132 | 2.567 | 3.153 | 3.989 |
| $X_t$ | MPa | 716.182 | 921.014 | 1125.845 | 1330.676 |
| $X_c$ | MPa | 416.646 | 428.703 | 442.481 | 456.274 |
| $Y_t$ | MPa | 41.244 | 41.504 | 42.095 | 42.739 |
| $Y_c$ | MPa | 84.272 | 84.804 | 86.011 | 87.328 |
| $S_L$ | MPa | 29.699 | 29.890 | 30.321 | 30.792 |
| $S_T$ | MPa | 31.752 | 31.952 | 32.407 | 32.903 |

A decrease in deflection and stable absorbed energy suggests less energy was absorbed by plastic deformation of the steel, and more energy was absorbed through composite damage. Thus, in terms of preventing damage to the metal substrate, increasing $V_f$ would be advantageous, but not as much as might be expected. Delaminations and adhesive disbonds were not substantially sensitive over this fiber volume range.

**Table 14. Comparison of FEA results for varying $V_f$**

| Data Type | Maximum Deflection (mm) | Percent Difference (%) | Maximum Contact Force (N) | Percent Difference (%) | Energy Absorbed (J) | Percent Difference (%) |
|---|---|---|---|---|---|---|
| $V_f$ = 0.3 | 3.99 | - | 5177.52 | - | 8.31 | - |
| $V_f$ = 0.4 | 3.87 | 2.84 | 5208.64 | 0.60 | 8.30 | 0.06 |
| $V_f$ = 0.5 | 3.78 | 5.41 | 5138.79 | 0.75 | 8.43 | 1.47 |
| $V_f$ = 0.6 | 3.68 | 8.08 | 5085.77 | 1.79 | 8.59 | 3.27 |

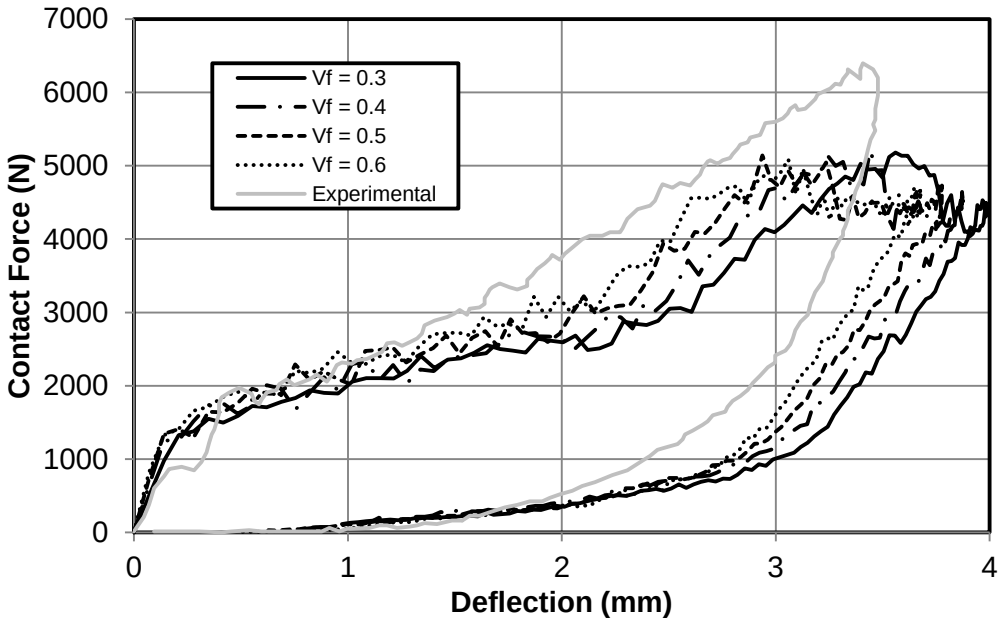


**Figure 35. Load-deflection curve for varying values of $V_f$**

## 5.3 Ply Thickness

Ply thickness was another uncertain parameter in this study. Akimoto et al. [52] did not provide the composite thickness in the validation paper. Only the steel, adhesive, and overall thicknesses were supplied. These numbers suggested that a thickness of 2.3 mm be used for the composite. However, in their follow-up paper, Akimoto et al. [53] used a similar setup with steel thickness at 0.5 mm, adhesive thickness at 0.2 mm, and composite thickness at 2.5 mm. The following study compared the performance of total composite thicknesses of 2.0 mm, 2.3 mm, 2.5 mm and 2.8 mm. Total thicknesses were divided by the four plies; the thickness of each ply increased accordingly.

Table 15 contains a comparison of the results of varying the ply thickness; Figure 36 contains the load-deflection curve. The results of increasing ply thickness were very similar to increasing the fiber content of the composite; both changes shifted the load-deflection curve to the left. Both maximum contact force and energy absorbed were insensitive to increasing the ply thickness. However, both were more sensitive to decreasing the ply thickness; with higher deflection, the steel absorbed more energy in the form of plastic deformation. Deflection was sensitive to all changes in thickness.

**Table 15. Comparison of FEA results for varying ply thickness**

| Thickness (mm) | Maximum Deflection (mm) | Percent Difference (%) | Maximum Contact Force (N) | Percent Difference (%) | Energy Absorbed (J) | Percent Difference (%) |
|---|---|---|---|---|---|---|
| 2.00 | 4.16 | 4.29 | 5294.38 | 2.23 | 8.54 | 2.72 |
| 2.30 | 3.99 | - | 5177.52 | - | 8.31 | - |
| 2.50 | 3.88 | 2.57 | 5137.64 | 0.77 | 8.34 | 0.43 |
| 2.80 | 3.72 | 6.85 | 5163.14 | 0.28 | 8.36 | 0.66 |

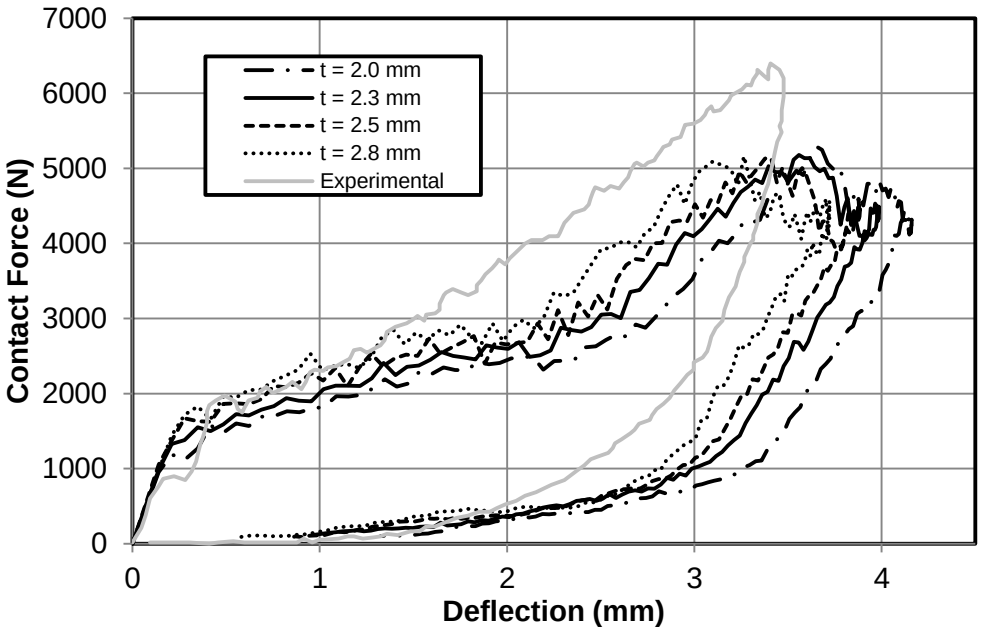


**Figure 36. Load-deflection curve for varying values of ply thickness**

## 5.4 Other Parameters

In addition to the parameters discussed above, several other uncertain parameters were also investigated. Mesh refinement was studied by comparing the validation results with results from a model with a 0.3 mm x 0.3 mm mesh at the impact site (Figure 37). To test the effect on the model of assuming the impactor to be a rigid body, a model was created modeling the impactor as quadratic continuum solid tetrahedral elements with stainless steel mechanical properties (Table 11). Several sets of Johnson-Cook plasticity parameters were found for SUS304 stainless steel. A model was created using a completely different set of parameters than used in the validation case; these material properties are provided in Table 16.

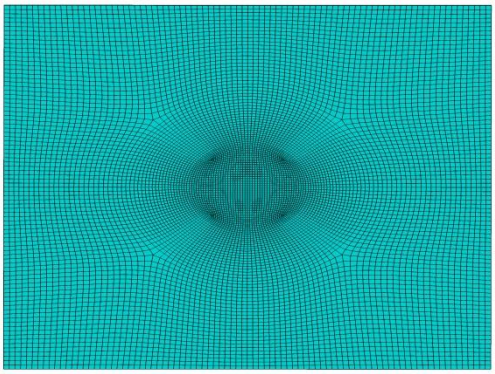

**Figure 37. Finer mesh for sensitivity analysis**

**Table 16. Material properties for SUS304 stainless steel – Option 2**

| Property | Units | Value | Source |
|---|---|---|---|
| E | GPa | 193 | [88] |
| G | GPa | 78 | [88] |
| v | - | 0.3 | [88] |
| ρ | g/cc | 8.03 | [88] |
| A | MPa | 310 | [89] |
| B | MPa | 1000 | [89] |
| n | - | 0.65 | [89] |
| C | - | 0.07 | [89] |
| Ref. Strain Rate | $s^{-1}$ | $10^{-2}$ | [89] |

Results from these three studies are gathered in Table 17 and Figure 38. The differences between the results for the validation and refined mesh case were negligible, which indicated that further ply mesh refinement was not worth the loss of computational efficiency. Nor did modeling the impactor with solid elements rather than as a rigid body make a notable difference. Using the other set of Johnson-Cook parameters yielded slightly less accurate results for deflection and contact force. However, these alternate

properties did yield a more accurate solution on energy absorption. None of these results differed enough from the validation case to warrant further investigation.

**Table 17. Comparison of FEA results for various parameters**

| Data Type | Maximum Deflection (mm) | Percent Difference (%) | Maximum Contact Force (N) | Percent Difference (%) | Energy Absorbed (J) | Percent Difference (%) |
|---|---|---|---|---|---|---|
| FEA - Validation | 3.986 | - | 5178 | - | 8.32 | - |
| FEA - Fine Mesh | 3.994 | 0.20 | 5185 | 0.14 | 8.51 | 2.27 |
| FEA - Solid Impactor | 3.992 | 0.15 | 5015 | 3.20 | 8.41 | 1.02 |
| FEA - Steel 2 | 4.066 | 2.03 | 4952 | 4.60 | 8.78 | 3.14 |

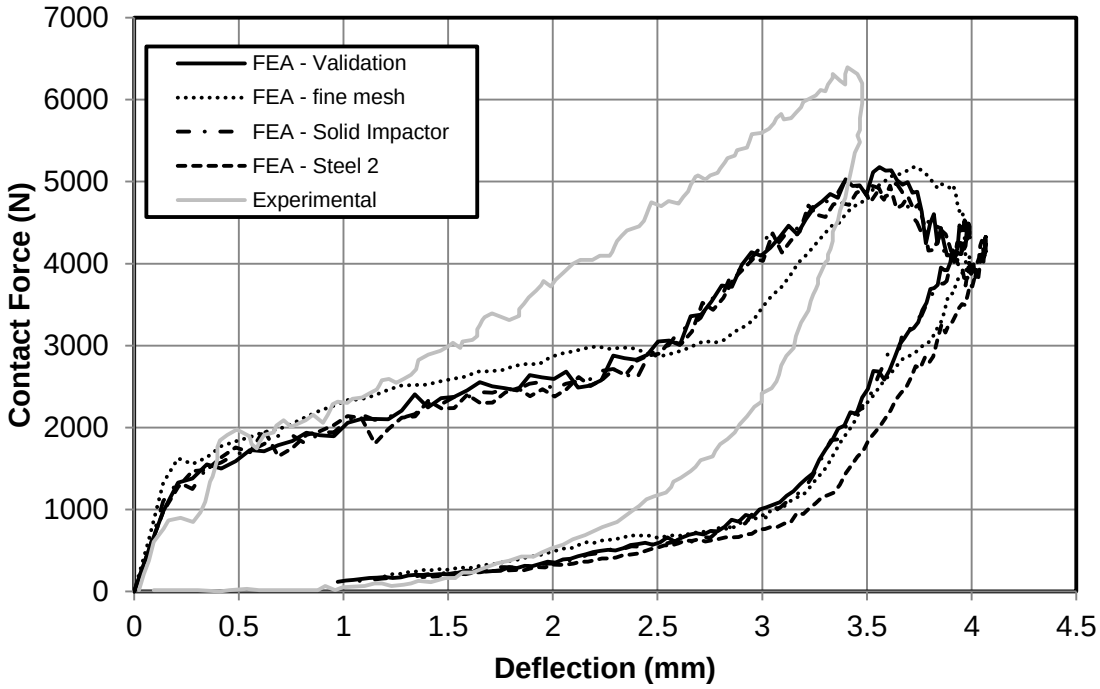


**Figure 38. Load-deflection curve for various parameters**

# CHAPTER VI

# CONCLUSIONS AND RECOMMENDATIONS

## 6.1 Strengths and Weaknesses of Model

Overall, the model performed well, both qualitatively and quantitatively, at predicting damage in a hybrid composite plate even with substantial uncertainty in the material and configuration input parameters. One of the most important factors in impact performance, energy absorption, was predicted within 7% of experimental data. The model behavior was generally less stiff than the experimental data indicated. The model under-predicted the level of contact force by 20%, while it over-predicted deflection by 14%. Determining the cause of this discrepancy was difficult with the limited test data available. Qualitatively, the damage predicted by this model in the form of ply damage, delamination, adhesive disbonding, and plastic metal deformation agreed with a range of experimental evidence. The validation model took about 3 hours to run; similar studies on composites have taken considerably longer [36].

Results from the sensitivity study are applicable to the problem of optimizing a composite patch for impact resistance. For example, if weight and profile were a design consideration, the analysis showed that increasing fiber volume might be a more effective method for improving impact performance than increasing the patch thickness.

However, this model has several weaknesses that require further investigation. First, the Hashin failure criteria have several inherent flaws that have already been discussed, especially concerning the compression criteria. The energy release rate based intralaminar damage evolution model is also troublesome. The proper input

values for the critical energy release rates ($G_f^t$, $G_f^c$, $G_m^t$, and $G_m^c$) are not obvious and are not easily calculated or obtained by established theory or experimentation, yet they have considerable influence on the behavior of the model. A model that calculates damage based on more tangible criteria would be preferable. The intralaminar model also does not take into account the *in situ* strength of the lamina, potentially resulting in an under-prediction of ply failure strain [63]. Nor does this model explicitly take into account the interplay between matrix cracking and delamination; instead, the model treats each as separate occurrences [40].

Secondly, the cohesive elements used for delamination required substantial analysis to achieve an acceptable data fit. Furthermore, cohesive properties had to be recalibrated with every change of materials. This manual curve fitting limits the ability of the user to quickly evaluate various combinations of fibers and matrices. The application of CZM to the adhesive was more straightforward as stiffness was based on actual material properties. While some research suggests that the value of $K$ is not critical if it is sufficiently large, this research indicated that for mixed-mode loading, the range of $K$ values giving acceptable answers was narrow and not easily pre-determined.

Another problem encountered in the model was hourglassing, as seen in Figure 39. This issue was encountered during the hybrid composite sensitivity study. The ply undergoing hourglassing would exhibit matrix tensile failure on one face of the continuum shell element and matrix compressive failure on the other face. Adding additional through-thickness elements exacerbated the problem as seen in the bottom half of Figure 39. The exact cause of this behavior has not been determined, but it warrants further examination.

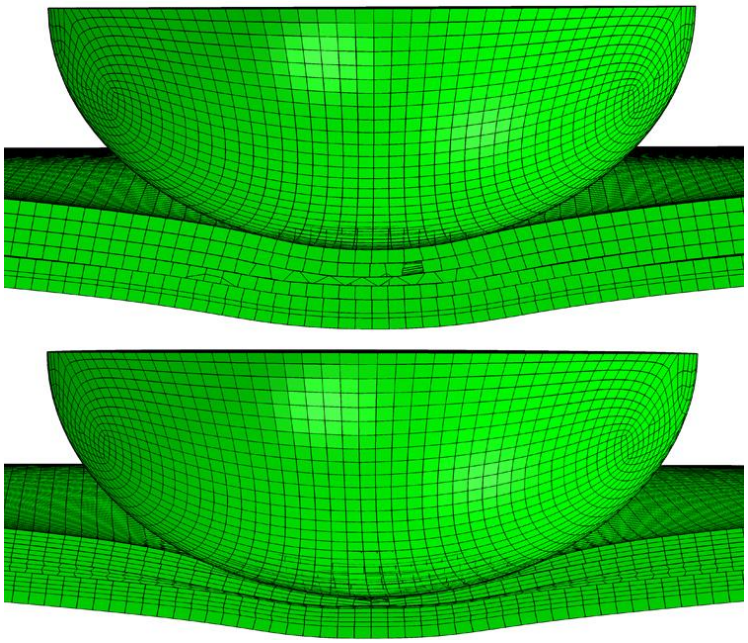

**Figure 39. Hourglassing in one element through thickness (top) and three elements through thickness (bottom)**

## 6.2 Future Work

It is recommended that the intralaminar composite damage model be revisited. In Abaqus, any revision to the damage model would have to take the form of a user created subroutine, or VUMAT. One such VUMAT is available from the creators of Abaqus, which incorporates more accurate compressive damage based on research by Puck and Schürmann [38]. This option also avoids the troublesome energy release rates needed for Lapcyzk's model. Additionally, the hourglassing problems encountered during this research could be avoided by using a damage model, like this VUMAT, which allows continuum solid elements. Another option would be to create a VUMAT based on another composite damage theory. However, creating or using a user-created

subroutine requires a more extensive knowledge of programming and the inner workings of Abaqus than the damage model presented in this research.

Another step would be to validate this model with additional experimental data. Then a comprehensive parameter study could be performed using this model to explore the sensitivity of the patch impact performance to number of plies, orientation of plies, fiber/matrix materials, adhesive type, metal thickness, etc. The problem size could be expanded to investigate edge effects and patch shape on a larger metal sheet with a patch. The damage models could also be modified to account for weaving, stitching, or z-pinning. Taking all these factors into account could lead to a more comprehensive optimal patch design as well as identify areas where more physical experimentation might be beneficial to further understand damage propagation and load redistribution.

# LIST OF REFERENCES

1. Baker, A.A., *Introduction and overview*, in *Advances in the bonded composite repair of metallic aircraft structure*, A.A. Baker, L.F. Rose, and R. Jones, Editors. 2003, Elsevier: Oxford, UK. p. 1-18.
2. Baker, A. and R. Jones, *Bonded repair of aircraft structures*. Vol. 7. 1988: Springer.
3. Hollaway, L. and J. Cadei, *Progress in the technique of upgrading metallic structures with advanced polymer composites.* Progress in Structural Engineering and Materials, 2002. **4**(2): p. 131-148.
4. De Freitas, M. and L. Reis, *Failure mechanisms on composite specimens subjected to compression after impact.* Composite Structures, 1998. **42**(4): p. 365-373.
5. Lapczyk, I. and J.A. Hurtado, *Progressive damage modeling in fiber-reinforced materials.* Composites Part A: Applied Science and Manufacturing, 2007. **38**(11): p. 2333-2341.
6. Hashin, Z., *Failure criteria for unidirectional fiber composites.* Transactions of the ASME. Journal of Applied Mechanics, 1980. **47**(2): p. 329-34.
7. Camanho, P.P., C. Davila, and M. De Moura, *Numerical simulation of mixed-mode progressive delamination in composite materials.* Journal of Composite Materials, 2003. **37**(16): p. 1415-1438.
8. Benzeggagh, M.L. and M. Kenane, *Measurement of mixed-mode delamination fracture toughness of unidirectional glass/epoxy composites with mixed-mode bending apparatus.* Composites Science and Technology, 1996. **56**(4): p. 439-449.
9. Turon, A., et al., *An engineering solution for using coarse meshes in the simulation of delamination with cohesive zone models.* NASA Technical Memorandum, 2005. **213547**.
10. Johnson, G.R. and W.H. Cook, *Fracture characteristics of three metals subjected to various strains, strain rates, temperatures and pressures.* Engineering Fracture Mechanics, 1985. **21**(1): p. 31-48.
11. Ouinas, D., et al., *Modelling of a cracked aluminium plate repaired with composite octagonal patch in mode I and mixed mode.* Materials & Design, 2009. **30**(3): p. 590-595.
12. Callinan, R.J. and S.C. Galea, *Bonded repair of acoustic fatigue cracking*, in *Advances in the bonded composite repair of metallic aircraft structure*, A.A. Baker, L.F. Rose, and R. Jones, Editors. 2003, Elsevier: Oxford, UK. p. 531-568.
13. Chester, R., *Case History: F-111 wing pivot fitting reinforcement*, in *Advances in the bonded composite repair of metallic aircraft structure*, A.A. Baker, L.F. Rose, and R. Jones, Editors. 2003, Elsevier: Oxford, UK. p. 813-842.
14. Bartholomeusz, R.A., P. Pearce, and R. Vodicka, *Rapid application technology: Aircraft battle damage repairs*, in *Advances in the bonded composite repair of metallic aircraft structure*, A.A. Baker, L.F. Rose, and R. Jones, Editors. 2003, Elsevier: Oxford, UK. p. 727-757.

15. Colombi, P., A. Bassetti, and A. Nussbaumer, *Crack growth induced delamination on steel members reinforced by prestressed composite patch.* Fatigue & Fracture of Engineering Materials & Structures, 2003. **26**(5): p. 429-438.
16. Schnerch, D., et al., *Proposed design guidelines for strengthening of steel bridges with FRP materials.* Construction and Building Materials, 2007. **21**(5): p. 1001-1010.
17. Shaat, A., et al. *Retrofit of steel structures using fiber-reinforced polymers (FRP): State-of-the-art*. in *Transportation research board (TRB) annual meeting. CD-ROM (04-4063)*. 2004.
18. Zhao, X.-L. and L. Zhang, *State-of-the-art review on FRP strengthened steel structures.* Engineering Structures, 2007. **29**(8): p. 1808-1823.
19. Bocciarelli, M., et al., *Fatigue performance of tensile steel members strengthened with CFRP plates.* Composite Structures, 2009. **87**(4): p. 334-343.
20. Colombi, P. and G. Fava, *Fatigue behaviour of tensile steel/CFRP joints.* Composite Structures, 2012. **94**(8): p. 2407-2417.
21. Teng, J., T. Yu, and D. Fernando, *Strengthening of steel structures with fiber-reinforced polymer composites.* Journal of Constructional Steel Research, 2012. **78**: p. 131-143.
22. Grabovac, I. and D. Whittaker, *Application of bonded composites in the repair of ships structures–A 15-year service experience.* Composites Part A: Applied Science and Manufacturing, 2009. **40**(9): p. 1381-1398.
23. Turton, T., J. Dalzel-Job, and F. Livingstone, *Oil platforms, destroyers and frigates—case studies of QinetiQ's marine composite patch repairs.* Composites Part A: Applied Science and Manufacturing, 2005. **36**(8): p. 1066-1072.
24. Shamsuddoha, M., et al., *Effectiveness of using fibre-reinforced polymer composites for underwater steel pipeline repairs.* Composite Structures, 2013. **100**: p. 40-54.
25. Chandekar, G.S., B.S. Thatte, and A.D. Kelkar, *On the Behavior of Fiberglass Epoxy Composites under Low Velocity Impact Loading.* Advances in Mechanical Engineering, 2010.
26. Shyr, T.-W. and Y.-H. Pan, *Impact resistance and damage characteristics of composite laminates.* Composite Structures, 2003. **62**(2): p. 193-203.
27. Malik, M.H., et al., *Impact resistance of composite laminate flat plates – A parametric sensitivity analysis approach.* Composite Structures, 2013. **102**: p. 138-147.
28. Hyung Yun, C., W. Hong Sheng, and F.K. Chang, *Effect of Laminate Configuration and Impactor's Mass on the Initial Impact Damage of Graphite/Epoxy Composite Plates Due to Line-Loading Impact.* Journal of Composite Materials, 1992. **26**(6): p. 804-827.
29. Belingardi, G. and R. Vadori, *Low velocity impact tests of laminate glass-fiber-epoxy matrix composite material plates.* International Journal of Impact Engineering, 2002. **27**(2): p. 213-229.

30. Lopes, C.S., et al., *Low-velocity impact damage on dispersed stacking sequence laminates. Part I: Experiments.* Composites Science and Technology, 2009. **69**(7–8): p. 926-936.
31. Evci, C. and M. Gulgec, *An experimental investigation on the impact response of composite materials.* International Journal of Impact Engineering, 2012. **43**: p. 40-51.
32. Kachanov, L., *Time of the rupture process under creep conditions.* Isv. Akad. Nauk. SSR. Otd Tekh. Nauk, 1958. **8**: p. 26-31.
33. Faggiani, A. and B.G. Falzon, *Predicting low-velocity impact damage on a stiffened composite panel.* Composites Part A: Applied Science and Manufacturing, 2010. **41**(6): p. 737-749.
34. Camanho, P.P. and C.G. Dávila, *Mixed-mode decohesion finite elements for the simulation of delamination in composite materials.* NASA-Technical Paper, 2002. **211737**(1): p. 33.
35. Kim, E.-H., et al., *Composite damage model based on continuum damage mechanics and low velocity impact analysis of composite plates.* Composite Structures, 2013. **95**: p. 123-134.
36. Guiamatsia, I., et al., *Enriched finite elements for the efficient prediction of impact-induced damage in composite laminates.* Composites Science and Technology, 2013. **79**: p. 87-96.
37. Shi, Y., T. Swait, and C. Soutis, *Modelling damage evolution in composite laminates subjected to low velocity impact.* Composite Structures, 2012. **94**(9): p. 2902-2913.
38. Puck, A. and H. Schürmann, *Failure analysis of frp laminates by means of physically based phenomenological models.* Composites Science and Technology, 1998. **58**(7): p. 1045-1067.
39. Berbinau, P., et al., *Effect of off-axis ply orientation on 0°-fibre microbuckling.* Composites Part A: Applied Science and Manufacturing, 1999. **30**(10): p. 1197-1207.
40. Raimondo, L., et al., *A progressive failure model for mesh-size-independent FE analysis of composite laminates subject to low-velocity impact damage.* Composites Science and Technology, 2012. **72**(5): p. 624-632.
41. González, E.V., et al., *Effects of ply clustering in laminated composite plates under low-velocity impact loading.* Composites Science and Technology, 2011. **71**(6): p. 805-817.
42. Koh, Y., et al., *Detection of disbonding in a repair patch by means of an array of lead zirconate titanate and polyvinylidene fluoride sensors and actuators.* Smart Materials and Structures, 2001. **10**(5): p. 946.
43. Soutis, C., D.M. Duan, and P. Goutas, *Compressive behaviour of CFRP laminates repaired with adhesively bonded external patches.* Composite Structures, 1999. **45**(4): p. 289-301.
44. Baker, A.A., *A proposed approach for certification of bonded composite repairs to flight-critical airframe structure.* Applied Composite Materials, 2011. **18**(4): p. 337-369.

45. Denney, J.J. and S. Mall, *Characterization of disbond effects on fatigue crack growth behavior in aluminum plate with bonded composite patch.* Engineering Fracture Mechanics, 1997. **57**(5): p. 507-525.
46. Al-Zubaidy, H.A., X.-L. Zhao, and R. Al-Mahaidi, *Dynamic bond strength between CFRP sheet and steel.* Composite Structures, 2012. **94**(11): p. 3258-3270.
47. Crocombe, A., et al., *Investigating fatigue damage evolution in adhesively bonded structures using backface strain measurement.* The Journal of Adhesion, 2002. **78**(9): p. 745-776.
48. Khalili, S.M.R., M. Shiravi, and A.S. Nooramin, *Mechanical Behavior of Notched Plate Repaired with Polymer Composite and Smart Patches - Experimental Study.* Journal of Reinforced Plastics and Composites, 2010. **29**(19): p. 3021-3037.
49. Khalili, S.M.R., et al., *An experimental study on the Charpy impact response of cracked aluminum plates repaired with GFRP or CFRP composite patches.* Composite Structures, 2009. **89**(2): p. 270-274.
50. Williams, T.S., et al., *Atmospheric pressure plasma effects on the adhesive bonding properties of stainless steel and epoxy composites.* Journal of Composite Materials, 2012.
51. Helms, J.E., G. Li, and S.-S. Pang, *Impact response of a composite laminate bonded to a metal substrate.* Journal of Composite Materials, 2001. **35**(3): p. 237-252.
52. Akimoto, H., et al., *Impact performance of macrocomposite laminates-1. Evaluation of energy absorbed in non-penetration impact test.* Journal of Reinforced Plastics and Composites, 2000. **19**(17): p. 1363-1378.
53. Akimoto, H., et al., *Impact performance of macrocomposite laminates-2. Effect of adhesive layers.* Journal of Reinforced Plastics and Composites, 2000. **19**(16): p. 1268-1292.
54. Zhu, S. and G.B. Chai, *Low-velocity impact response of fibre–metal laminates – Experimental and finite element analysis.* Composites Science and Technology, 2012. **72**(15): p. 1793-1802.
55. Fan, J., Z.W. Guan, and W.J. Cantwell, *Numerical modelling of perforation failure in fibre metal laminates subjected to low velocity impact loading.* Composite Structures, 2011. **93**(9): p. 2430-2436.
56. Maimí, P., et al., *A thermodynamically consistent damage model for advanced composites.* NASA TM Technical Reports, 2006. **214282**.
57. Nakatani, H., et al., *Damage characterization of titanium/GFRP hybrid laminates subjected to low-velocity impact.* Composites Part A: Applied Science and Manufacturing, 2011. **42**(7): p. 772-781.
58. Reyes V, G. and W.J. Cantwell, *The mechanical properties of fibre-metal laminates based on glass fibre reinforced polypropylene.* Composites Science and Technology, 2000. **60**(7): p. 1085-1094.
59. Dávila, C.G. and P.P. Camanho, *Failure criteria for FRP laminates in plane stress.* NASA TM, 2003. **212663**(613).

60. Bazant, Z.P. and B.H. Oh, *Crack band theory for fracture of concrete.* Materials and Structures, 1983. **16**: p. 155-177.
61. Matzenmiller, A., J. Lubliner, and R.L. Taylor, *A constitutive model for anisotropic damage in fiber-composites.* Mechanics of Materials, 1995. **20**(2): p. 125-152.
62. Soden, P., M. Hinton, and A. Kaddour, *Lamina properties, lay-up configurations and loading conditions for a range of fibre-reinforced composite laminates.* Composites Science and Technology, 1998. **58**(7): p. 1011-1022.
63. Barbero, E.J., et al., *Determination of material parameters for Abaqus progressive damage analysis of E-glass epoxy laminates.* Composites Part B: Engineering, 2013. **46**(0): p. 211-220.
64. Davila, C.G., P.P. Camanho, and C.A. Rose, *Failure criteria for FRP laminates.* Journal of Composite materials, 2005. **39**(4): p. 323-345.
65. Mi, Y., et al., *Progressive delamination using interface elements.* Journal of Composite Materials, 1998. **32**(14): p. 1246-1272.
66. Song, K., C.G. Dávila, and C.A. Rose. *Guidelines and parameter selection for the simulation of progressive delamination*. in *abaqus User's Conference, Newport, Rhode Island* 2008.
67. Yang, Q. and B. Cox, *Cohesive models for damage evolution in laminated composites.* International Journal of Fracture, 2005. **133**(2): p. 107-137.
68. Harper, P.W. and S.R. Hallett, *Cohesive zone length in numerical simulations of composite delamination.* Engineering Fracture Mechanics, 2008. **75**(16): p. 4774-4792.
69. Corigliano, A., *Formulation, identification and use of interface models in the numerical analysis of composite delamination.* International Journal of Solids and Structures, 1993. **30**(20): p. 2779-2811.
70. Hui, C.-Y., et al., *Crack blunting and the strength of soft elastic solids.* Proceedings of the Royal Society of London. Series A: Mathematical, Physical and Engineering Sciences, 2003. **459**(2034): p. 1489-1516.
71. Hillerborg, A., M. Modéer, and P.-E. Petersson, *Analysis of crack formation and crack growth in concrete by means of fracture mechanics and finite elements.* Cement and Concrete Research, 1976. **6**(6): p. 773-781.
72. Alfano, G. and M.A. Crisfield, *Finite element interface models for the delamination analysis of laminated composites: mechanical and computational issues.* International Journal for Numerical Methods in Engineering, 2001. **50**(7): p. 1701-1736.
73. *Abaqus 6.12 Analysis User's Manual*. Abaqus 6.12 Documentation. 2012: Dassault Systems.
74. *Standard Test Method for Mixed Mode I-Mode II Interlaminar Fracture Toughness of Unidirectional Fiber Reinforced Polymer Matrix Composites*. 2006, ASTM International: West Conshohocken, PA.
75. Reeder, J.R. and J.R. Crews, *Mixed-mode bending method for delamination testing.* AIAA Journal, 1990. **28**(7): p. 1270-1276.

76. Campilho, R.D.S.G., et al., *Modelling adhesive joints with cohesive zone models: effect of the cohesive law shape of the adhesive layer.* International Journal of Adhesion and Adhesives, 2013. **44**(0): p. 48-56.
77. Abou-Hamda, M.M., M.M. Megahed, and M.M.I. Hammouda, *Fatigue crack growth in double cantilever beam specimen with an adhesive layer.* Engineering Fracture Mechanics, 1998. **60**(5–6): p. 605-614.
78. Da Silva, L., V. Esteves, and F. Chaves, *Fracture toughness of a structural adhesive under mixed mode loadings.* Materialwissenschaft und Werkstofftechnik, 2011. **42**(5): p. 460-470.
79. de Moura, M.F.S.F., R.D.S.G. Campilho, and J.P.M. Gonçalves, *Pure mode II fracture characterization of composite bonded joints.* International Journal of Solids and Structures, 2009. **46**(6): p. 1589-1595.
80. da Silva, L.F., et al., *Mode II fracture toughness of a brittle and a ductile adhesive as a function of the adhesive thickness.* The Journal of Adhesion, 2010. **86**(9): p. 891-905.
81. Mohotti, D., et al., *Out-of-plane impact resistance of aluminium plates subjected to low velocity impacts.* Materials & Design, 2013. **50**(0): p. 413-426.
82. Cadoni, E., L. Fenu, and D. Forni, *Strain rate behaviour in tension of austenitic stainless steel used for reinforcing bars.* Construction and Building Materials, 2012. **35**(0): p. 399-407.
83. Grytten, F., et al., *Low velocity perforation of AA5083-H116 aluminium plates.* International Journal of Impact Engineering, 2009. **36**(4): p. 597-610.
84. Price, J.N. and D. Hull, *Effect of matrix toughness on crack propagation during stress corrosion of glass reinforced composites.* Composites Science and Technology, 1987. **28**(3): p. 193-210.
85. Eckold, G.C., et al., *Lamination theory in the prediction of failure envelopes for filament wound materials subjected to biaxial loading.* Composites, 1978. **9**(4): p. 243-246.
86. Daniel, I. and O. Ishai, *Engineering Mechanics of Composite Materials, 2nd Edition*. New York: Oxford University Press, Inc. 411.
87. Szekrényes, A. and J. Uj, *Advanced beam model for fiber-bridging in unidirectional composite double-cantilever beam specimens.* Engineering Fracture Mechanics, 2005. **72**(17): p. 2686-2702.
88. *Product Data Sheet: 304/304 Stainless Steel*. 2007, AK Steel Corporation: West Chester, Ohio.
89. Dean, J., et al., *Energy absorption during projectile perforation of thin steel plates and the kinetic energy of ejected fragments.* International Journal of Impact Engineering, 2009. **36**(10–11): p. 1250-1258.
90. Barbero, E.J., *Introduction to Composite Materials Design*. 2011: CRC press.

# APPENDIX

## A.1 Derivation of Material Properties

The transverse shear strength of the lamina may be determined from:

$$S_T = Y_c \cos\alpha_0 \left(\sin\alpha_0 + \frac{\cos\alpha_0}{\tan 2\alpha_0}\right) \tag{A1}$$

The fracture angle ($\alpha_0$) was assumed to be 53° [64].

Due to the unusually low fiber-volume ratio present in the validation case for impact on a composite/metal hybrid, lamina material properties had to be generated from fiber and matrix properties. The following equations, along with Equation A1 provide the elastic material properties [86]:

$$E_1 = V_f E_{1f} + V_m E_m \tag{A2}$$

$$E_2 = E_m \frac{(1+V_f)E_{2f} + V_m E_m}{V_m E_{2f} + (1+V_f)E_m} \tag{A3}$$

$$\nu_{12} = V_f \nu_{12f} + V_m \nu_m \tag{A4}$$

$$G_{12} = G_m \frac{(1+V_f)G_{12f} + V_m G_m}{V_m G_{12f} + (1+V_f)G_m} \tag{A5}$$

$$E_2 = E_3, \qquad G_{12} = G_{13}, \qquad \nu_{12} = \nu_{13} \tag{A6-A8}$$

$$\nu_{23} = 1 - \frac{E_2}{K_2} - 2\nu_{12}^2 \frac{E_2}{E_1} \tag{A9}$$

$$G_{23} = \frac{G_m\left[K_m(G_m + G_{23f}) + 2G_{23f}G_m + K_m(G_{23f} - G_m)V_f\right]}{K_m(G_m + G_{23f}) + 2G_{23f}G_m - (K_m + 2G_m)(G_{23f} - G_m)V_f} \tag{A10}$$

$$K_m = \frac{E_m}{2(1+\nu_m)(1-2\nu_m)} \tag{A11}$$

$$K_2 = \frac{(K_{2f} + G_m)K_M + (K_{2f} - K_m)G_m V_f}{(K_{2f} - G_m) - (K_{2f} - K_m)V_f} \tag{A12}$$

$$K_f = \frac{E_{1f}E_{2f}}{2(1-\nu_{23f})E_{1f} - 4\nu_{12f}^2 E_{2f}} \tag{A13}$$

The next set of equations predicts the lamina strength characteristics [90]:

$$X_t = X_{tf}V_f + X_{tf}\frac{E_m}{E_f}\left(1 - V_f\right) \tag{A14}$$

$$X_c = G_{12}(1 + 4.76\chi)^{-0.69} \tag{A15}$$

$$\chi = \frac{G_{12}\alpha_\sigma}{S_L} \tag{A16}$$

$$Y_t = Y_{tm}C_v\left[1 + \left(V_f - \sqrt{V_f}\right)\left(1 - \frac{E_m}{E_f}\right)\right] \tag{A17}$$

$$Y_c = Y_{cm}C_v\left[1 + \left(V_f - \sqrt{V_f}\right)\left(1 - \frac{E_m}{E_f}\right)\right] \tag{A18}$$

$$C_v = 1 - \sqrt{\frac{4V_v}{\pi\left(1 - V_f\right)}} \tag{A19}$$

$$S_L = S_{Lm}C_v\left[1 + \left(V_f - \sqrt{V_f}\right)\left(1 - \frac{G_m}{G_{12f}}\right)\right] \tag{A20}$$

The volume of voids ($V_v$) was assumed to be 1%. The standard deviation of fiber misalignment ($\alpha_\sigma$) was assumed to be 3.4°.

## A.2 DCB Theoretical Solution

The theoretical solution employed for the DCB tests was found in Mi et al. [65]. This solution is composed of two sections: the linear elastic portion until crack initiation, reflecting cantilever behavior of the plies, and the crack propagation. For the linear elastic portion, the load, $F$, applied to the end of the beam is given by:

$$F = \frac{3E_1I\Delta}{2a_0^3} \tag{A21}$$

In this equation, Δ represents deflection of one arm, $a_0$ is the initial crack length, and $I$ is the moment of inertia of one arm. The curve corresponding to the crack propagation behavior of the DCB is given as:

$$\Delta = \frac{2}{3}\frac{(BG_{Ic}EI)^{3/2}}{EIF^2} \tag{A22}$$

$B$ represents the width of the specimen.

## A.3 MMB Theoretical Solution

The theoretical solution for the MMB tests is provided by ASTM D6671 [74]. The results of Equations A23-A29 provide the force and displacement of the tip of the lever arm. This value was compared to the results of the FEA in Figure 13, Figure 14, and Figure 15. Equations A23 and A24 provide values for $\Gamma$, the transverse modulus correction parameter, and $\chi$, the crack length correction parameter:

$$\Gamma \equiv 1.18\frac{\sqrt{E_1E_2}}{G_{12}}; \quad \chi \equiv \sqrt{\frac{E_1}{11G_{13}}\left\{3 - 2\left(\frac{\Gamma}{1+\Gamma}\right)^2\right\}} \tag{A23, A24}$$

Equation A24 calculates the force on the lever arm, $F_{lever}$.

$$F_{lever} = \sqrt{\frac{\frac{4}{3}G_cB^2E_1h^3L^2}{(3d-L)^2(a+h\chi)^2 + \frac{3}{4}(d+L)^2(a+0.42h\chi)^2}} \tag{A25}$$

In this equation $L$ denotes the length of the specimen, $B$ the width, $h$ the thickness of one arm, and $a$, the crack length. Note $G_c$ is calculated from the BK mixed mode law, Equation 32 based on the mode mixity ratio, $G_{II}/G_T$. The mode mixity ratio is itself based on the length of the lever arm, $d$, shown in Equations A26 - A28.

$$d = \frac{12\beta^2 + 3\alpha + 8\beta\sqrt{3\alpha}}{36\beta^2 - 3\alpha}L, \tag{A26}$$

$$\alpha = \frac{1 - \frac{G_{II}}{G_T}}{\frac{G_{II}}{G_T}}; \qquad \beta = \frac{\alpha + \chi h}{\alpha + 0.42\chi h} \tag{A27, A28}$$

Finally, the displacement of the tip of the lever arm is given by:

$$\Delta_{lever} = \frac{F_{lever}}{8BE_1 h^3 L^2}[4(3d - L)^2(a + h\chi)^3 + (d + L)^2(2L^3 + 3(a + 0.42h\chi)^3)] \tag{A29}$$

# VITA

Geoffrey Goodmiller was born in Clarksville, Tennessee, on 11 December 1983, to Roy E. Goodmiller and Carole L. Hargrove. After graduating from Dickson County High School, he went on to earn his Bachelor of Architecture degree from the University of Tennessee at Knoxville in May 2007. He worked as an intern architect on healthcare design projects for the next two years before returning to the University of Tennessee in 2009 to study civil and structural engineering. Upon earning a Bachelor of Science in Civil Engineering in May 2012, Geoff immediately began working his Master of Science degree. While pursuing this degree, he primarily conducted research on damage in fiber composites using finite element analysis.